1994A&A...292..543F

Astron. Astrophys. 292, 543–568 (1994)

ASTRONOMY AND ASTROPHYSICS

Multi-site continuous spectroscopy

II. Spectrophotometry and energy budget of exceptional white-light flares on HR 1099 from the MUSICOS 89 campaign*

B.H. Foing[1,2], S. Char[2,3], T. Ayres[4], C. Catala[5], J.E. Neff[6], D.S. Zhai[7], S. Catalano[8], G. Cutispoto[8], S. Jankov[2], M. Rodono[8], T. Simon[9], C. Akan[10], A. Aslanov[11], P. Avellar[12], J. Baudrand[5], H. Beust[13], H. Cao[7], H. Chatzichristou[5], J.G. Cuby[5], J. Czarny[5], R. de la Reza[14], M. Dreux[5], P. Felenbok[5], R. Ferlet[13], A. Frasca[8], M. Floquet[5], K. Ghosh1[5], Z. Guo[7], J. Guérin[5], J.X. Hao[7], E.R. Houdebine[2,16], L. Huang[7], A.M. Hubert[5], H. Hubert[5], J. Huovelin[17], J. Hron[18], C. Ibanoglu[11], S. Jiang[7], V. Keskin[11], A.M. Lagrange-Henri[13,19], J.M. Lecontel[20], Q. Li[7], L. Mavridis[21], R. Nolthenius[22], P. Petrov[23], I. Savanov[23], A. Scherbakov[23], I. Tuominen[17], A. Vidal-Madjar[13], R. Zhang[7], and X. Zhang[7]

[1] ESA Solar System Division, Space Science Department, ESTEC (SO), Postbus 299, NL-2200 AG Noordwijk, The Netherlands
[2] Research Network in Space Science and Astrophysics (ICARUS), Europe and Institut d'Astrophysique Spatiale CNRS, France
[3] Universidad de La Serena, Chile
[4] CASA, Boulder, USA
[5] Observatoire de Paris-Meudon, France
[6] Penn State University, USA
[7] Beijing Astronomical Observatory, China
[8] Osservatorio di Catania and Istituto di Astronomia, Catania, Italy
[9] University of Hawaii, USA
[10] Izmir Astronomy institute, Turkey
[11] Tashkent Observatory CIS
[12] National Solar Observatory, USA
[13] Institut d'Astrophysique de Paris, France
[14] National Observatory, Rio de Janeiro, Brazil
[15] Vainu Bappu Observatory, India
[16] Armagh Observatory, UK
[17] Helsinki Observatory, Finland
[18] Vienna Observatory, Austria
[19] Observatoire de Grenoble, France,
[20] Observatoire de la Côte d'Azur, France
[21] Thessaloniki Observatory, Greece
[22] Cabrillo College, USA
[23] Crimea Astrophysical Observatory, CIS

Received 18 May 1992 / Accepted 25 March 1994

Abstract. We report results from the December 89 multi-site continuous observing campaign (MUSICOS 89) dedicated to the study of surface active structures and flares on the RS CVn-type system HR 1099 (= V711 Tau). This system has been observed by up to 17 telescopes around the globe during this campaign. We obtained complete phase coverage for Doppler imaging of photospheric spots. Quasi-simultaneously, we observed the modulation of Ca II K line profile due to chromospheric plage regions. At least two exceptional white-light flares on 14 Dec. 15:00 UT and 15 Dec. 1:00 UT (the largest such optical flare episode ever reported in a RS CVn system) were detected photometrically with typical rise and decay times of 60–90 min, and with remarkable spectral dynamic signatures in Hα, with longer decay time scale. Equivalent colours, temperature excesses and projected flare areas (0.55 and 0.89 solar disc areas) were derived for the two optical flares. We estimate the energy budget for these two events, with respective peak intensities of radiative losses of 1.65 and 14 10^{33} erg s^{-1} and integrated losses over the white-light event duration of a few hours of 8 10^{36} and

Send offprint requests to: B.H. Foing (ESA/ESTEC address)

* Based on observations obtained during the MUSICOS 89 MUlti-SIte COntinuous Spectroscopic campaign from ESO La Silla, NSO Mac Math, Canada France Hawaii, Univ. Hawaii, Beijing Astronomical Observatory (BAO) Xinglong, Crimea, Catania and Haute-Provence (OHP) telescopes, and on data obtained with the International Ultraviolet Explorer

© European Southern Observatory • Provided by the NASA Astrophysics Data System

1994A&A...292..543F

10^{38} ergs (in the 3100–5900 Å range), indicating a total energy balance several times these values. The emission was also measured in the Hα and Hβ lines during these flares with a ratio of flare optical emission over Balmer emission 3–4 times larger compared to other flares on dwarfs. More than one day after the last white-light flare, part of the flare decay phase was also measured with IUE in UV lines of low and high excitation; the extrapolated transition region EUV losses are found similar to the derived Balmer line losses. Both flares were shown to occur near the limb. We derive their physical area, and estimate their densities, column mass, and penetration depth. From Balmer line broadening and flows, we derive a kinetic energy budget comparable to the radiative losses. We discuss a possible magnetic energy budget and the interpretation in terms of filament ejection occurring over a magnetic arcade. These observations bring a new understanding and questions about energy transport mechanisms in stellar flares.

Key words: stars: activity of – stars: binaries: spectroscopic – stars: flare – stars: late-type – stars: individual: HR 1099 – stars: imaging

1. Introduction

The wave-like variations in the optical light curves of rapidly rotating late-type stars, in particular the RS CVn variables, can be interpreted in terms of cool surface spots analogous to sunspots. Associated with the modulation of optical light are variations in the strengths of chromospheric and transition region lines, which generally are in antiphase with the optical light curve (Rodonò et al. 1986, 1987). This is reminiscent of a solar-like model where magnetic structures overlaying the photospheric spots give rise to excess heating of the outer atmosphere (Byrne et al. 1987).

The RS CVn-type systems are chromospherically active binary stars, one of whose components is a G-K subgiant or giant (Hall 1981). This component shows very strong Ca II H & K emission, is rotating rapidly, and has quasi-sinusoidal brightness variations. The magnetic activity of these systems appears to be due to enhanced dynamo effect resulting from the coupling between the higher rotation rate due to synchronisation and the cool star convective motions.

Flares on RS CVn systems are quite often detected in the radio regime (e.g. see review by Mullan 1985). These radio flares can last for up to days and involve a characteristic size up to several stellar radii. They are therefore events taking place within a substantial fraction of the low density corona. Ultraviolet and optical emission line and microwave flares lasting typically several hours also have been recorded. Linsky et al. (1988) recorded a major ultraviolet and radio flare on the star HR 1099 lasting at least 6 hours. Density sensitive line ratios and emission measures showed that at temperatures of around 10^5 K, the electronic density was 10^{11} cm^{-3} and the flaring volume was 10^{30} cm^3. Wide-band optical flare events in RS CVn systems have not been convincingly reported, because only very energetic flares could be detected against the bright photospheric background of G and K stars.

A method known as Doppler imaging, was proposed by Vogt and Penrod (1983) and further applied to RS CVn stars by several authors (e.g. Jankov & Foing 1992, 1993). It uses the Doppler shifted signature of localised structures on line profiles, to reconstruct an image of photospheric spots at the stellar surface. The measurements of the spot signatures at various rotational phases indicate the location of spots in longitude and latitude. A method for chromospheric spectral imaging has been also used for Mg II lines observed by IUE (Neff et al. 1988) and extended to the Ca II (Char & Foing 1989) or Hα lines (Foing et al. 1990, 1993).

An important constraint on the activity of these systems is to obtain the large scale distribution of the magnetic field and associated structures on these active stars (Foing et al. 1990). Doppler imaging of these systems in different lines (from the photosphere to the corona) can give a 3 dimensional picture of extended and stratified magnetic structures, and information on the conditions of their equilibrium and instability. Continuous and flare-like processes responsible for the chromospheric and coronal non-thermal emission can be also studied in these very active systems, in particular their relation with the configuration and distribution of the magnetic field. The spectrophotometric monitoring of these systems can provide information on the dynamics, energy balance and transport mechanisms during flare events (Foing 1989). Thus, tomographic imaging of magnetic structures and the monitoring of flaring were the two key science objectives of the MUSICOS campaign for the selected target V711 Tau. A further description of the scientific background and rationale for multi-site campaigns on RS CVn systems can be found in the review by Neff (1990). We recall previous results and parameters related to HR 1099 (Sect. 2), present the specific objectives of the HR 1099 MUSICOS 89 campaign (Sect. 3). We give the overview of ground-based multi-site spectroscopic observations (Sect. 4), ultraviolet observations with IUE (Sect. 5). We discuss the measured rotational modulation from photometry/spectroscopy of spots and plages (Sect. 6), photometric observations, flare radiative losses, Hα spectroscopy and IUE post-flare measurements of 14 and 15 December of white-light flares (Sects. 7, 8, 9) and finally interpret (Sect. 10) the temporal variation in continua and Balmer line radiative losses, and the kinetic energy budget in the context of magnetic arcades and flare energy transport in RS CVn stars.

2. The HR 1099 (= V711 Tauri) system

V711 Tau (= HR 1099) is a bright, variable (V = 5.7–5.9) non-eclipsing RS CVn system of spectral type K1 IV + G5 IV/V, with orbital period 2.83774 days, heliocentric conjunction time HJD = 244 2766.080. Average color indices are respectively: $U - B$ = 0.46, $B - V$ = 0.92, $V - R$ = 0.77 and $R - I$ = 0.39. Fekel (1983) has made a series of assignations for the spectral types of the two components to fit the observed V magnitude and color indices of HR 1099. For the G5

© European Southern Observatory • Provided by the NASA Astrophysics Data System

1994A&A...292..543F

V+ K0 IV assignation, corresponding effective temperatures are 5500 K and 4750 K, and absolute magnitudes are respectively 4.2 and 3.7. High quality radial velocity observations lead to a mass ratio of 1.25. The derived star separation is 11.5 $R_\odot$ in solar radius units and the inclination is 33 degrees. On the basis of measured rotational broadening (with respective vsini of 13 and 38 km s^{-1}), Fekel estimated the radii of components $R_1 = 1.3\,R_\odot$ and $R_2 = 3.9\,R_\odot$. However, a recent photometric solution by Zhai et al. (1994) leads to both components above the main sequence with the G5 star closer to the G5 IV type than to the G5 V type of Fekel (1983). For the Roche model photometric solution of Zhai et al. (1994), the respective temperatures are 5370 K and 4620 K, and derived masses are 1.1 and 1.4 solar mass.

HR 1099 was detected as a radio source by Owen et al. (1976), and it has shown several strong radio outbursts. Such outbursts may be related to the rapid change of spot characteristics. Its intrinsic light variability was reported by Bopp et al. (1977). Chromospheric and transition region lines have been detected in the UV with IUE, and variable X-ray emission has been reported (Walter et al. 1978). A photometric study by Bartolini et al. (1983), based on five years observations at different sites, showed remarkable variability of the photometric wave. They concluded that the changes in the light curves are consistent with rearrangements of the spot distribution over the stellar surfaces, rather than sizeable changes of the integrated activity level. More recent studies, based on the entire collection of photometry of HR 1099 (Cutispoto 1990; Cutispoto & Rodonò 1992) have pointed out that some degree of variability in the global degree of photospheric spottedness is present. Spot modelling based on light curves has shown that up to 20% of the surface of the active K1 IV component can be covered by spots (Rodonò et al. 1987).

3. Science rationale and objectives for the HR 1099 MUSICOS 89 campaign

The main objectives of this campaign were to obtain information on active surface structures on this RS CVn system, through the observed spectroscopic rotational modulation, to measure the spectral signature and dynamics of flares, and to constrain further models and interpretation theories.

3.1. MUSICOS objectives for HR 1099: Doppler imaging and flare monitoring

Requests for the MUSICOS programme on *Doppler imaging of active structures* were:

(a) to observe unblended photospheric lines suitable for Doppler imaging (Ca I and Fe I lines at 6430 and 6439 Å) at 12 to 15 phases during the rotation period,

(b) to register simultaneously the photometric modulation due to spots,

(c) to measure quasi-simultaneously the spectral signature of chromospheric structures such as solar-like plages in the Ca II K line,

(d) to measure the effect of active coronal structures (possibly vertically extended) in the Hα line.

A flare monitoring patrol was also achieved for the following goals:

(a) to disentangle flare-induced enhancements of emission lines from those due to rotational modulation by magnetic structures, such as plages,

(b) to study over different wavelength regimes any flare event (photometrically and spectroscopically) in order to assess the radiative energy budget,

(c) to monitor the system in the Hα line continuously in order to study the spectroscopic signature of violent flares and diagnosis of flare dynamics, mass ejections and flows, and

(d) to study the link between flare build-up and the configuration of the magnetic field.

3.2. MUSICOS spectroscopic observation planning

These scientific goals require continuous observations ideally covering at least 2 rotational periods of the system in order to distinguish transient phenomena from the rotational modulation. As a minimum compromise within the overall MUSICOS campaign, three complete days (about one orbital period) were dedicated to this multi-site programme, but additional data were obtained at a few sites around the MUSICOS window, such as Ca II K spectrometry (Char et al. 1990, 1993) and photometry obtained over many rotation periods at Xinglong and La Silla sites (Zhai et al. 1990, 1994; Char 1992).

Instructions for the spectroscopic observations were sent to the participants before the campaign. The two scientific programmes on HR 1099 (surface imaging and flare monitoring) required a different temporal coverage strategy:

– *Surface imaging* with at least 1 high quality spectrum centered at 6430 Å per site per night for photospheric Doppler imaging and 1 spectrum with the Ca II K line for those sites equipped for this range. The observing strategy was to obtain spectra with S/N over 200, with exposures between 30 and 60 min, and at the highest possible spectral resolution with a minimum of 30 000.

– *Flare monitoring* with a continuous sequence of short exposures in the region around Hα. This required resolution in the range 30 000, typical exposure times of 15 min with a maximum allowed of 30 min, and the highest S/N possible (with minimum 50).

The same calibration and comparison stars were used at all sites, in order to correct the data for some instrumental effects in the continuum response and in the resolution. The B3 V star HR 3454 was observed in the various wavelength ranges in order to correct for telluric absorption (especially water in the Hα range) and for instrumental slopes. The stars HR 3762 and HR 4182 (of similar spectral types G6IV and K1IV as the components of V711 Tau) were also observed as immaculate and inactive slow rotating stars. These reference spectra were used in synthetic Doppler imaging methods and for assessing the excess chromospheric/coronal emission in V711 Tau. They

© European Southern Observatory • Provided by the NASA Astrophysics Data System

1994A&A...292..543F

Table 1. Sites, telescopes and equipment of the instruments involved in the HR 1099 campaign

Site	Telescope	Instrument	Detector	Resolution	Obs. dates
Hawaii US	2.2m UH	ISISbis	TI 800×800	50000	Dec.14
Hawaii	3.6m CFH	Coudé	Ford516×516	35000	Dec.15–16
Kitt Peak	1.5m MacMath	Coudé	TI 800×800	40000	Dec.15
La Silla, ESO	1.4m CAT	CES	THX CCD	50000	Dec.14–16
La Silla, ESO	1m ESO	Special Ca II	Intensified reticon 128	13000	Dec. 5–20
OHP, France	1.52m OHP	Aurélie	Linear THX	40000	No observations
Etna, Italy	0.91m La Nave	Low dispersion	EEV385×576	3700	Dec.14–19
Crimea	2.6m Shajn	Coudé	GEC 576×385	50000	No observations
Xinglong, China	2.16m	ISIS	THX 576×384	30000	Dec.14–17
Space	IUE	LWP-HI SWP-LO	Vidicon 300	10000	Dec.16–17
La Silla, ESO	50 cm ESO	Photometer	UBV (RI)c		Nov. 28–Dec. 26
Greece	80 cm Stephanion	Photometer	UBV		Dec.14–18
China	60 cm Xinglong	Photometer	UBV+Hβ		Nov.9–Dec.26

also gave information on the instrumental performances, resolution and Modulation Transfer Function, and about instrument variations. The star EI Eri was proposed as a secondary target, easier for testing the Doppler imaging method (since it is a single spectrum spectroscopic SB1 binary) to be applied for the first time to such a heterogeneous set of data.

4. Description of the HR 1099 MUSICOS 89 campaign

4.1. Overview

A summary of the operations of the MUSICOS 89 campaign can be found in Catala & Foing (1990) and Catala et al. (1993). MUSICOS (MUlti SIte COntinuous Spectroscopy) is a project whose goal is to facilitate multi-site multi-wavelength observations in stellar spectroscopy. The project was born from the needs of many scientific programs, in particular those related to stellar magnetic activity, winds and oscillations. These require continuous spectroscopic observations from 2m class telescopes giving a good longitude coverage around the globe. These goals further required the following steps: (1) to organise multi-site campaigns with existing instruments and transportable spectrographs; (2) to define, design and build an echelle spectrograph meeting the science requirements; (3) to duplicate this spectrograph and operate it on a network of 2m class telescopes around the world.

The MUSICOS December 1989 campaign, relevant to the first step, was a multi-site, multi-program campaign. There were three scientific programmes co-ordinated by three principal investigators (PI's): Intrinsic Variability of Be stars (PI, A.M. Hubert), Streams in the Winds of Herbig Ae/Be stars (PI, C. Catala) and Surface Structures and Flares of RS CVn systems (PI, B.H. Foing). Here, we shall report only on the scientific results from the RS CVn programme on HR 1099. The original plan, which was gradually set up starting in the summer of 1988, was to observe the three stars from 6 sites, indicated in Catala et al. (Table 1). The French ISIS spectrograph (Felenbok & Guérin 1987) was mounted on the 2.16m telescope at Xinglong. Observations in Hawaii were first made on the UH 2.2 m telescope, where a similar spectrograph (ISIS-bis) had been transported, and then followed by two nights at CFHT, with observations of fast Ca II K spectral variations. The different performances of the MUSICOS core campaign spectroscopic instruments are further described in Catala et al. (1993). For the HR 1099 observations, specific observations at ESO used the ESO CES (Coudé Echelle Spectrometer) at Coudé Auxiliary Telescope (1.4 m CAT) with remote control from Garching (Jankov et al. 1990), and the special IAP/IAS Ca II spectrometer installed at ESO 1m telescope (Char et al. 1990). Table 1 gives the information about the telescopes involved in the HR 1099 spectroscopic and photometric campaign.

Figure 1 shows the distribution of participating sites on the Earth. Additional observations coordinated with the campaign included: ultraviolet spectroscopy from the IUE satellite, visible spectroscopy from Catania (Italy) and Vainu Bappu (India) observatories, and visible photometry from Xinglong, ESO La Silla and other observatories world-wide.

4.2. Summary of the HR 1099 spectroscopic observations

From the different sites, we list in Table 2 the spectra of HR 1099 that have been obtained, either in the 6430/6439 Å lines used for photospheric Doppler imaging (PDI), in the spectral range including Hα, or in the Ca II K line range.

In addition, 25 Ca II K spectra with the special IAP/IAS spectrometer were obtained with a resolution of 0.4 Å, with excellent phase coverage over the period from 5 to 20 December (cf. Char et al. 1990; Char et al. 1993). The 13 Ca II K spectra obtained from CFHT explored fast time variations near the phase of conjunction.

The spectroscopic temporal coverage of HR 1099 had a duty cycle of only 70% as two sites (Crimea and OHP) could not obtain data due to clouds (cf. Fig. 1b). The phase coverage in the high resolution (30 000–60 000) and high signal/noise ob-

© European Southern Observatory • Provided by the NASA Astrophysics Data System

1994A&A...292..543F

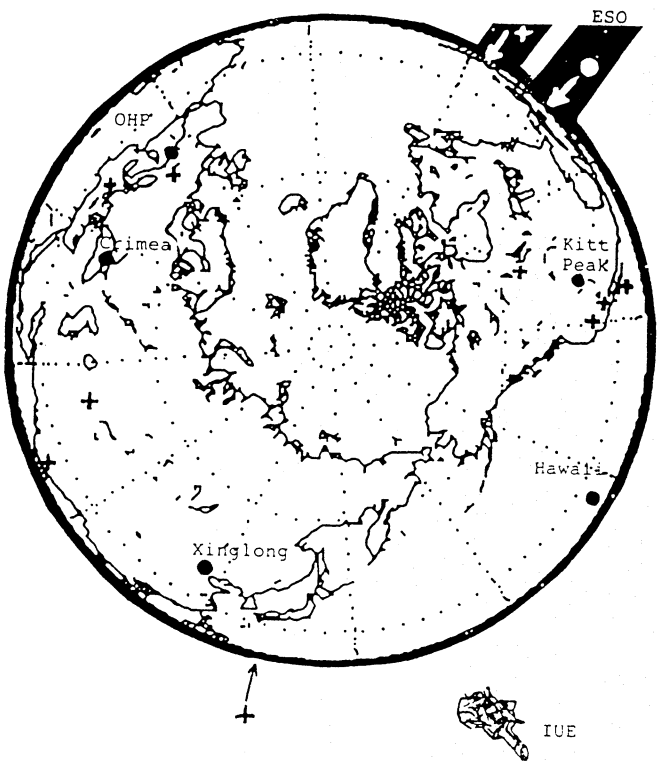

Fig. 1a. The distribution on Earth of the sites involved in the MUSICOS 89 campaign. Filled circles indicate sites involved in the original plan: Xinglong (XL), Crimea, OHP, ESO La Silla, Mac Math NSO (Mc), Hawaii (UH), + symbols represent photometric and additional sites (Australia, India, USSR, Turkey, Greece, Catania, Austria, Brazil, Canada, US and Mexico) and the IUE satellite is also represented. The distribution provides a good longitude coverage with some redundancy east of Hawaii and west of Crimea

servations of the photospheric lines at 6430 Å and 6439 Å was completed during the 14–16 December MUSICOS campaign, except for significant gaps at phases 0.44–0.53, 0.72–0.84 and 0.92–1.01. However, for the Hα spectroscopy, we had additional low resolution spectra from the La Nave Etna site. From the whole data set, we were fortunate to catch 2 exceptional flares for which an analysis is presented in this paper.

4.3. Reduction of the data

A detailed description of the data reduction and extraction techniques specific or common to the various participating spectroscopic sites is given in Appendix A of Catala & Foing (1990) and in Catala et al. (1993) (Paper I). The primary data reduction was performed mainly at the VAX-8600 of Paris-Meudon Observatory using the eVe software developed at Paris-Meudon Observatory. For data from Kitt Peak, Hawaii UH 2.2, Hawaii CFHT, and Xinglong obtained on a 2D detector, the background was subtracted both from stellar spectra and flat-field spectra by interpolating between smoothed averages of 10 columns on both sides of the spectrum. Pixels affected by cosmic ray hits were replaced by an interpolation between adjacent pixels. All spectrographs used had no cross-dispersion, providing single order spectra that can be simply extracted (with no problems of distortions, S-shapes or echelle ripple). The 1D extraction and averaging from the 2D images was dependent on the site, since the image slicers and CCD binning parameters were different (cf. Paper I). The 1D stellar spectra were then divided by the 1D flat field spectra. This procedure is justified when the flat field spectrum falls exactly at the same CCD location as the stellar spectra. If it is not the case, a more sophisticated method should be used. The wavelength calibration was performed after slice extraction and averaging. We checked that in all cases line inclination resulted in negligible loss of spectral resolution. The wavelength calibration introduced a slight resampling of the spectra. Spectra were normalised to continuum unity for the 6430 and 6563 Å ranges. For the Ca II K ESO spectra, the data reduction and flux calibration are described in Char et al. (1993).

The IHAP reduction and data analysis package was used finally at ESTEC (and partly at ESO) for the measurements on the reduced spectra, on which the following analysis is based. The equivalent widths (EW) were first measured in a fixed wavelength interval, and showed a modulation due to the orbital velocity variations of the profiles of the binary components. For an accurate and homogeneous data set, we measured the EW in the velocity reference frame of the primary star in order to study phenomena associated with this star. The EW were computed by considering the excess emission with respect to a local continuum interpolated by a linear fit to line-free nearby continuum portions included within the covered spectral interval. The EW measurements are relatively free of blend from photospheric lines, except at the spectral resolution of the Etna La Nave spectrograph, for which a special correction for photospheric line contribution was made.

5. Ultraviolet observations of HR 1099 during the MUSICOS campaign

5.1. IUE observation sequences and strategy

We observed HR 1099 with the IUE satellite during two 8-hour observing shifts (NASA No. 2) on 1989 December 16 and 17 (UT). We returned to HR 1099 on 1990 February 3 to obtain an additional sequence of LWP high-resolution spectra at a phase opposite to that of the December 16 series. A catalogue of the exposures is provided in Table 3. Our observations on December 16 began about 26 hours after the onset, and 25 hours after the peak, of the giant flare described in the next sections.

The primary goal of our program was to obtain very-high signal-to-noise profiles at high dispersion of the Mg II and Mg I uv1 resonance lines in the 2800 Å region to support the multi-wavelength Doppler-imaging objective of the MUSICOS campaign. We also obtained a number of short wavelength (1150–1950 Å) low dispersion spectra, primarily to document any flare activity, although our program as a whole was not designed specifically as a flare patrol. We set the exposure lengths so that part of the obligatory read- and preparation-cycle overhead for the long wavelength echelle exposures could be "hidden" during the SWP observations (and likewise we read and prepared the

© European Southern Observatory • Provided by the NASA Astrophysics Data System

1994A&A...292..543F

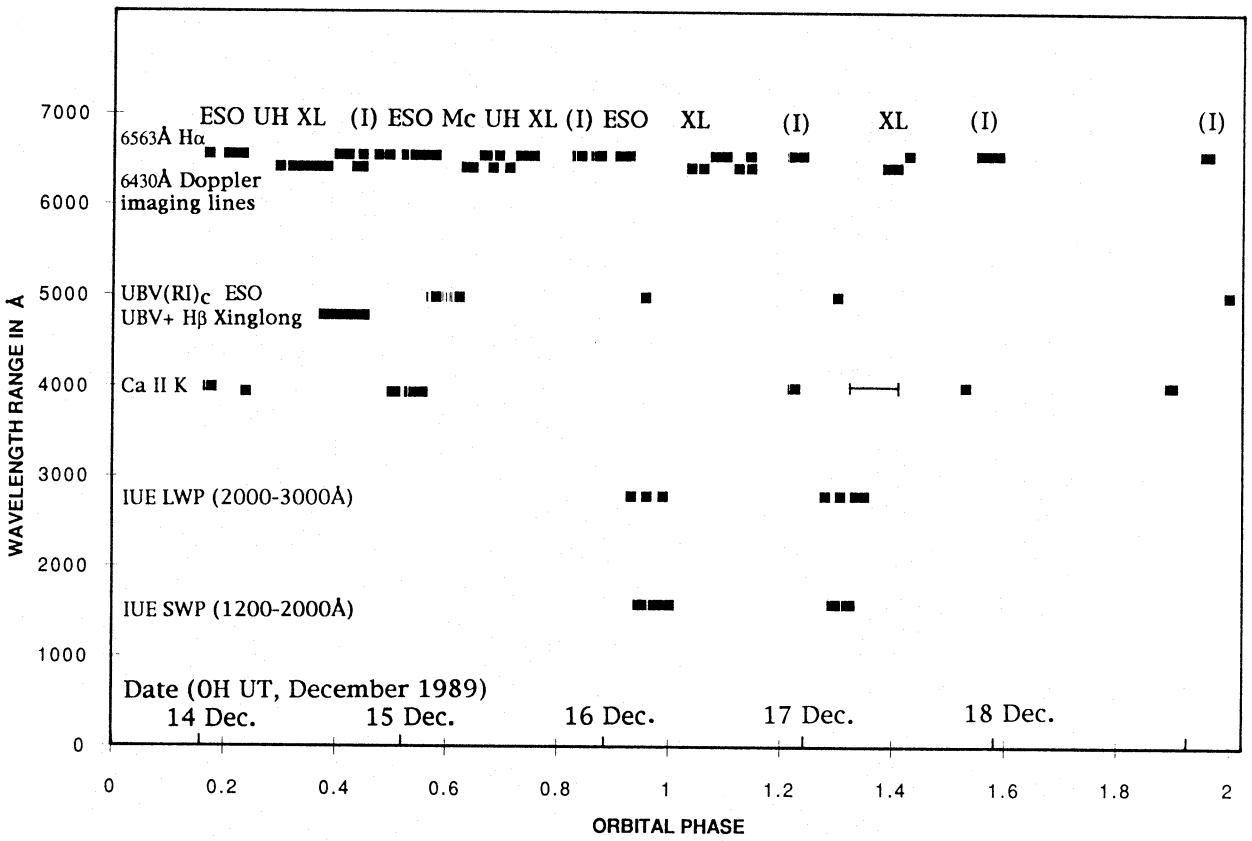

Phase for conjunction (J.D.Hel.)=2442766.080+2.83774*E

Fig. 1b. In the lower figure is given the coverage in unfolded phase (increasing from beginning to end of the campaign) of HR 1099 obtained from the MUSICOS 89 core spectroscopic sites at high resolution for the two prime wavelength domains at Hα and for photospheric Doppler imaging. The duty cycle is about 70% with some limited phase gaps due to poor weather conditions in OHP/Crimea. The Hα coverage was completed at low spectral resolution at phases 0.5 and 0.85 from the Etna site (I). The photometric coverage either in UBV or UBVRI is also indicated. The IUE coverage on 16 Dec. 6:00 UT and 17 Dec. 6:00 UT corresponds to phases 0.95 and 1.3 on this diagram

Table 2. Summary of the MUSICOS core spectroscopic instruments coverage either in the 6430/6439 A lines used for photospheric Doppler imaging (PDI), in the range including Hα, or in the Ca II K line range. The number of individual spectra are given for each instrument and observing day

	Date			
Site	14-12-1989	15-12-1989	16-12-1989	17-12-1989
ESO	2 PDI+ 6 Hα	2 PDI+ 9 Hα	2 PDI+ 7 Hα	
MacMath		4 PDI+ 7 Hα		
UH	2 PDI	2 PDI+ 3 Hα		
CFHT			13 Ca II K	
China	2 PDI+ 3 Hα	1 PDI+ 3 Hα	3 PDI+ 3 Hα	2 PDI (+ 1 Hα)
Crimea	Clouds	Clouds	Clouds	Clouds
Catania	9 Hα	7 Hα	6 Hα	6 Hα
OHP	Clouds	Clouds	Clouds	Clouds

SWP camera during the LWP exposures). For most of the SWP low-resolution spectra, we obtained "pseudo-trailed" 15 min exposures at each of two discrete offset reference points. We chose positions (see Table 3) 5″ from the centre of the 10″ × 20″ large aperture along the long axis (which is perpendicular to the dispersion line in the low-resolution mode). The spatial separation of the double spectra is sufficient to permit them to be measured individually, thereby allowing some time discrimination: the end of the first sub-exposure and the beginning of the sec-

© European Southern Observatory • Provided by the NASA Astrophysics Data System

1994A&A...292..543F

Table 3. Catalogue of IUE observations in support of MUSICOS on HR 1099

Camera image No.	Dispersion	Exposure (min)	Obs. start time (UT)
1989 DOY 350 (Dec. 16 post-flare)			
LWP 16928	H	45	03:45 (B)
SWP 37828	L	2 × 15	04:41 (B); 05:08 (A)
LWP 16929	H	2 × 10	05:40 (A')
SWP 37829	L	2 × 15	06:35 (A); 07:06 (B)
LWP 16930	H	2 × 10	07:39 (B')
SWP 37830	L	15	08:29 (C)
1989 DOY 351 (Dec. 17 post-flare)			
LWP 16931	H 45	03:27 (B)	
SWP 37834	L	2 × 15	04:21 (B); 04:45 (C)
LWP 16932	H	2 × 10	05:18 (A')
SWP 37835	L	2 × 15	06:09 (A); 06:32 (B)
LWP 16933	H	2 × 10	07:08 (B')
LWP 16934	H	36	08:12 (A)
1990 DOY 034 (1990 Feb. 3 comparison)			
LWP 17287	H	2 × 10	19:45 (A')
LWP 17288	H	2 × 10	20:48 (B')
LWP 17289	H	67	21:59 (C)

Notes: Observer: T.R. Ayres; Program ID: CSLTA; all observations through 10″ × 20″ aperture. Offset reference points (FES coordinates): A= (+05,−216) ; B= (−37,−208); C= (−16,−208) [normal centre]; A' = (+05,−208) & (+05,−224); B'= (−37,−200) & (−37,−216).

ond were separated by the approximately 10 minutes required for repositioning the stellar image.

The LWP echelle exposures were taken using a strategy to maximise signal-to-noise and dynamic range. The exposures were grouped in sequences containing two general types: (1) *relatively short double* exposures (2 × 10 min again pseudo-trailed perpendicular to the dispersion), and (2) one, or more, *deep point-source spectra*, usually taken at one of the positions located 5″ on either side of the aperture centre along the long axis (see SWP-LO above) but in one case at the aperture centre. The short LWP observations were designed to yield unsaturated fluxes of both Mg II components; the pseudo-trailed exposures provide increased dynamic range and higher S/N (by spreading the recorded signal over more Vidicon pixels). For the echelle mode the dispersion runs along the long axis of the aperture, thus the pseudo-trailing must be along the short axis. To avoid clipping either of the images at the edge of the aperture, we chose image positions separated by only 4″ (comparable to the FWHM of the telescope point spread function). The partial blending of the doubled spectra prevents an assessment of the temporal behaviour, unlike the SWP-LO case described previously. In principle, the pseudo-trailing can slightly degrade the spectral resolution if the images are not located exactly perpendicular to the dispersion, but in practice the random positioning errors usually correspond to only a few km s^{-1}, or less, which is negligible compared with the roughly 30 km s^{-1} resolution in the LWP-HI mode.

In practice, we obtained the short LWP-H I exposures in groups of two (usually separated by an SWP-LO: see Table 3): the first with the double image offset, located 5″ to one side of the aperture centre or the other (see Table 3). The motivation for offsetting the two spectra was to enhance the S/N of a coadded spectrum through the suppression of any "fixed patterns" in the photometric linearisation and to eliminate transient defects through "difference filtering" (see, e.g., Ayres et al. 1986). Again, our primary objective was to obtain very high quality spectral material for Doppler imaging purposes, rather than optimise the observations for a flare patrol. In that regard, the deeper point-source observations were designed to record the fainter wings of the Mg II profiles as well as the comparatively weak Mg I emission core.

When possible, the deep exposures, as well as the shorter pseudo-trails, were taken at positions offset from the aperture centre, again to reduce the fixed-pattern noise and to permit the application of the difference-filter strategy. The exposure times for the deep observations nominally were 45-minutes, although the final exposure of a sequence was lengthened or shortened to fill the remaining time in the observing shift.

5.2. Photometric linearisation and spectral extraction of IUE spectrograms

We applied a standard reduction procedure to the LWP echellograms based on the IUESIPS "MEHI" file provided to the Guest Observer. The nominal rectangular extraction profiles used by the IUESIPS are sufficiently broad at the echelle orders containing the Mg I and Mg II lines (m = 81–83) that one can extract reliably the widened images in the short, pseudo-trailed exposures. We applied a new, state-of-the-art reduction procedure to the SWP low-dispersion images. We photometrically linearised the raw images using an Intensity Transfer Function based on the 1985 recalibration of the SWP camera; identified and removed point-like cosmic-ray hits and other transient defects using an automated procedure; derived, and subtracted, an off-spectrum background by spatially-filtering and heavily smoothing the fluxes in reference bands above and below the spectral swath; and extracted the stellar spectrum using an "Optimal" weighted slit, like that described by Kinney et al. (1991), based on the local cross-dispersion profile of the spectral trace and a "noise model" that assigns a photometric uncertainty to each pixel flux according to its intensity. The Optimal extraction explicitly accounts for spatially-extended spectral traces like the double exposures of HR 1099, and is designed to track the spatial "undulations" of the spectrum which result from shears in the camera's fiber-optic coupler. This allowed us to add coherently the spectral information, to filter out specifically the noise, and to improve the wavelength accuracy without appreciable loss of spectral resolution.

© European Southern Observatory • Provided by the NASA Astrophysics Data System

1994A&A...292..543F

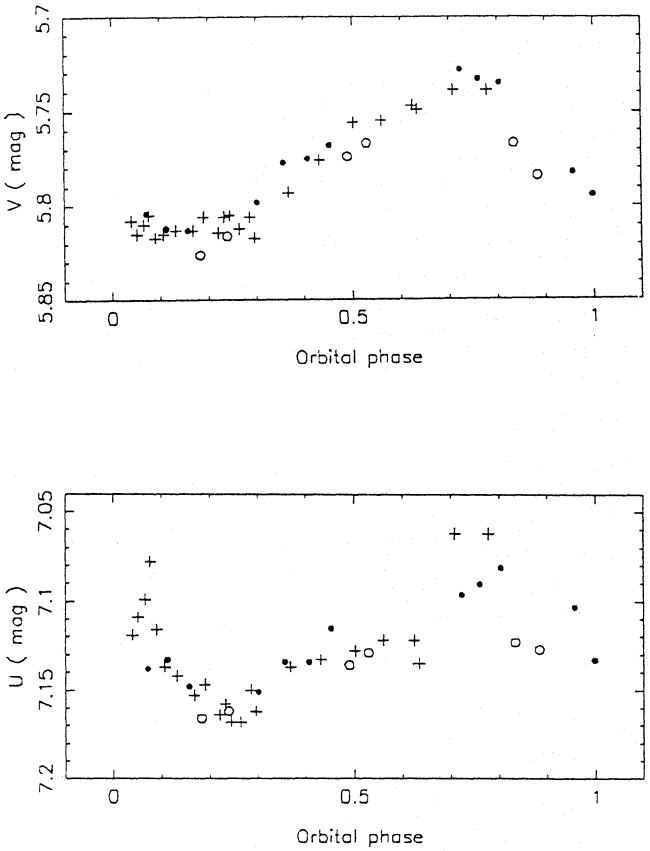

Fig. 2. V and U photometry obtained at different sites outside the core MUSICOS spectroscopic campaign corresponding to Xinglong (crosses), and to ESO 50 cm La Silla before (open circles) and after (filled circles) the giant 14/15 December flare. The data show the rotational modulation due to surface photospheric spot inhomogeneities. In the U band discrepant measurements at a given phase correspond to different dates and are indicative of flaring activity

6. Rotational modulation by surface structures

6.1. Photometry

Photometry was obtained at different sites before, during and after the MUSICOS campaign, the most complete coverage was obtained from Xinglong (in U, B, V) and from ESO La Silla (in the Cousins system U, B, V, R_c, I_c) (Figs. 2 and 3). Also at Xinglong, Hβ measurements using narrow/broad band filters were simultaneously obtained. The photometric light curve in U, B and V bands, obtained at Xinglong from 9 Nov. to 26 Dec. presents from this single site a gap of 0.2 in phase, while using data for both sites fills this gap and gives redundancy before, during and after the MUSICOS spectroscopic campaign. All of data secured on 8 nights was synthesised into the light curves using the ephemerides given by Fekel (1983). The distortion wave has an amplitude of 0.07 mag. in V, with the minimum brightness at phase 0.18 and the maximum near phase 0.75. The asymmetrical light curve is indicative of a distribution with more than a single spot in the surface. A preliminary photometric solution using a 2-spot model for only the B and V light curves

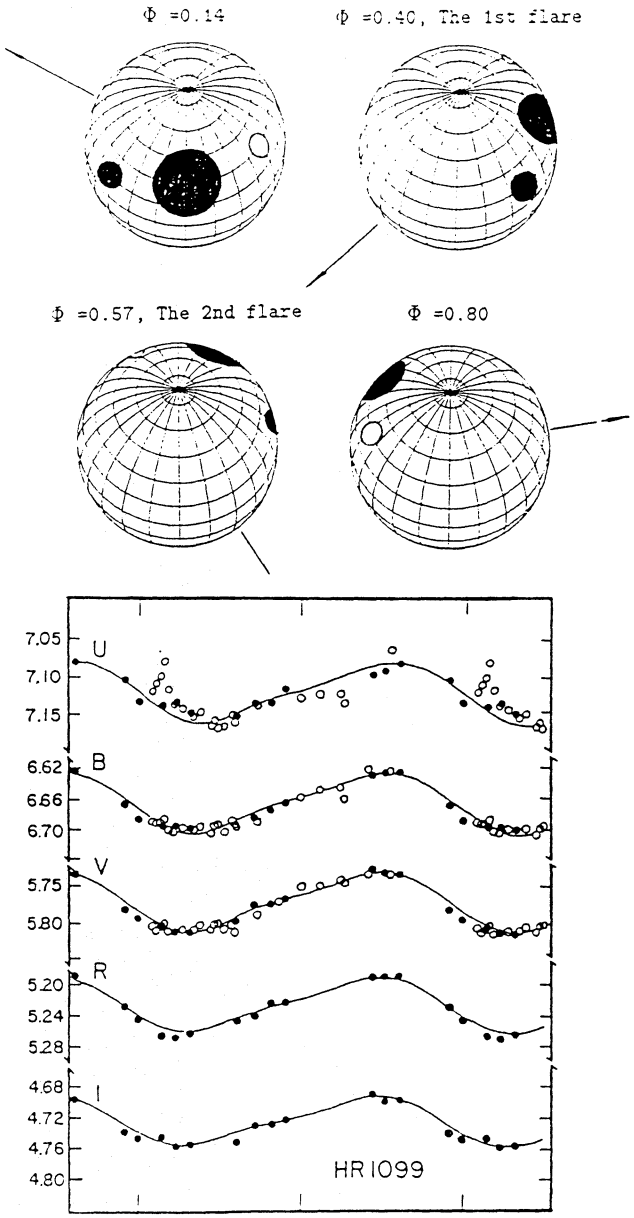

Fig. 3. Reconstructed photometric light curve vs. orbital phase with a model using a spot distribution with 1 hot spot (open circle) and 2 cool spots (filled circles) from Zhai et al. (1994). The points at phases around 0.07 and 0.75 correspond to flares and have not been included in the spot model adjustment. The corresponding surface map gives the spot positions and equivalent extent

(Zhai et al. 1990) gave 2 spots with the following parameters (latitude and radius in degrees):

	Latitude (deg)	Transit phase	Radius (deg)	T_{spot}/T_{phot}
Spot A	33	0.236	25	0.77
Spot B	23	0.66	9	0.90

Complete light curves including both Xinglong and ESO 50 cm photometry outside the core spectroscopic MUSICOS

© European Southern Observatory • Provided by the NASA Astrophysics Data System

1994A&A...292..543F

campaigns have been produced (Fig. 3) confirming the shape attributed to rotational modulation by spotted structures. Some dispersion in the U band photometry data points for the same phase indicates the presence of flaring or short term variability. The light curves show an unusual phase shift of light minimum between the different wave bands. Also, we shall see that the MUSICOS campaign corresponded to an episode of giant flaring, and we measure a systematic change between the photometry before and after this episode. It is found from a complete photometric analysis and spot modelling (Zhai et al. 1994) that the characteristics of the $UBV(RI)c$ light curve from ESO and Xinglong sites can be reconstructed with two cool spots plus one spot preceding them that was slightly cooler than the photosphere before the flare, but became hotter during the several days after the giant flare (Zhai et al. 1994). The derived positions with formal errors (in parenthesis) from the photometric solution given by Zhai et al. (1994) are:

	Latitude (deg)	Transit phase	Radius (deg)	T_{spot}/T_{phot}
Hot spot 1	30.5 (0.3)	0.973	8.4 (.1)	1.16
Cool spot 2	29.3 (0.3)	0.145	20.8 (0.8)	0.83
Cool spot 3	25.7 (1.8)	0.286	7.8 (0.3)	0.71

The formal uncertainties are small, but express only the convergence properties of the parametric solution based on 3 circular spots, taking into account the residuals from the light curve fitting. The parametric solution is therefore very dependent on the a priori assumptions, and cannot be considered a unique solution to this ill-posed problem. The comparison between solutions assuming 2 or 3 spots indicates the dependence of such photometric reconstructions, on the model. However the 3 spot solution is much better constrained, since it makes use of all of the UBV(RI) data from ESO and Xinglong, and it can be useful for deriving equivalent average global photometric properties of the surface inhomogeneities.

6.2. *Signature of spots in photospheric lines*

From line profiles of the Ca I and Fe I lines at 6430 and 6439 Å, obtained at different phases from the different sites, we obtained a radial velocity curve that allows to distinguish the signature of the two stellar components, and their orbital displacements. The signature of photospheric spots appear as bumps in the rotationally broadened profile ($v \sin i = 38\,\mathrm{km\,s^{-1}}$) of the primary star, the more active of the system. The importance of this kind of contiguous phase coverage is that it can provide a snapshot image of the photospheric spots and inhomogeneities in a time possibly shorter than the time scales for evolution of these structures. To obtain a similar phase coverage for HR 1099 from a single site requires a time span of 14 days (5 times the 2.8 day rotation period) during which the spot configuration and size may change significantly. Phase completeness and homogeneity of the data set are critical for the success of the Doppler imaging programme. Also a check between stationary and transient structures would require observations covering more than 2 rotational periods. The photospheric line coverage for the MUSICOS 89 campaign is in principle satisfactory, but it covers only about one rotational period without redundancy, which was due to the operational limit of 3 full days for the campaign.

Another difficulty is the inhomogeneity of the multi-site data in spectral resolution, systematic effects and S/N. We used comparison stars for checking and intercomparing the instrument performances. Also the range of spectral resolution (from 6 to $10\,\mathrm{km\,s^{-1}}$) and the final S/N (80–150) were not as good as expected due to weather conditions and instrument limitations. This would allow in principle a maximum typical resolution of 4–6 elements along the primary radius with a moderate reliability. From a previous data set obtained in September 1988 from 27 CES + reticon spectra with resolution $4\,\mathrm{km\,s^{-1}}$ and S/N over 200, Jankov & Foing 1993 could reconstruct a map with more than 10 resolution elements along the primary star radius, and at a significantly lower noise than for the MUSICOS data set. Since HR 1099 is a SB2 binary, the orbital shift of the secondary star can create spurious structures at given phases if instrumental systematic corrections are not properly done. A quite unexpected problem in the Doppler imaging programme arose from the large phase interval during the MUSICOS campaign during which there were giant white-light flares. These flares with temporal variations much shorter than the rotation period alter not only the continuum level from the primary but also its photospheric line profiles due to chromospheric filling and possible hot spot broad band emission from the flare area (Zhai et al. 1994).

The positions found from the photometric modelling are close to the two large high latitude spots derived from the Doppler imaging reconstruction of Jankov and Foing (1993) based on spectroscopic data from September 1988. However, more rigorous reconstructions taking into account the character of the MUSICOS data and the various described effects differ significantly from the preliminary solution and are more dependent on the physical and modelling assumptions. In particular, the contamination of the photospheric profiles by chromospheric (Char et al. 1993) and flare effects (this paper) must be estimated before one can make a Doppler imaging reconstruction. The processed and homogenised photospheric data are analysed by several independent groups for applying Doppler imaging codes, and thus obtaining and comparing the spot distribution. For the above reasons, the results of the complete Doppler imaging modelling analysis will be reported in a forthcoming paper using and comparing different techniques applied to this complex data set.

6.3. *Signature of chromospheric plages in the Ca II K line*

A series of Ca II K spectra were obtained by using a special spectrometer developed in collaboration between the Institut d'Astrophysique de Paris and the Institut d'Astrophysique Spatiale (IAP/IAS), and installed on the ESO 1m telescope during December 1989. The series of spectra allow good coverage of the chromospheric flux modulation associated with the visibility

© European Southern Observatory • Provided by the NASA Astrophysics Data System

1994A&A...292..543F

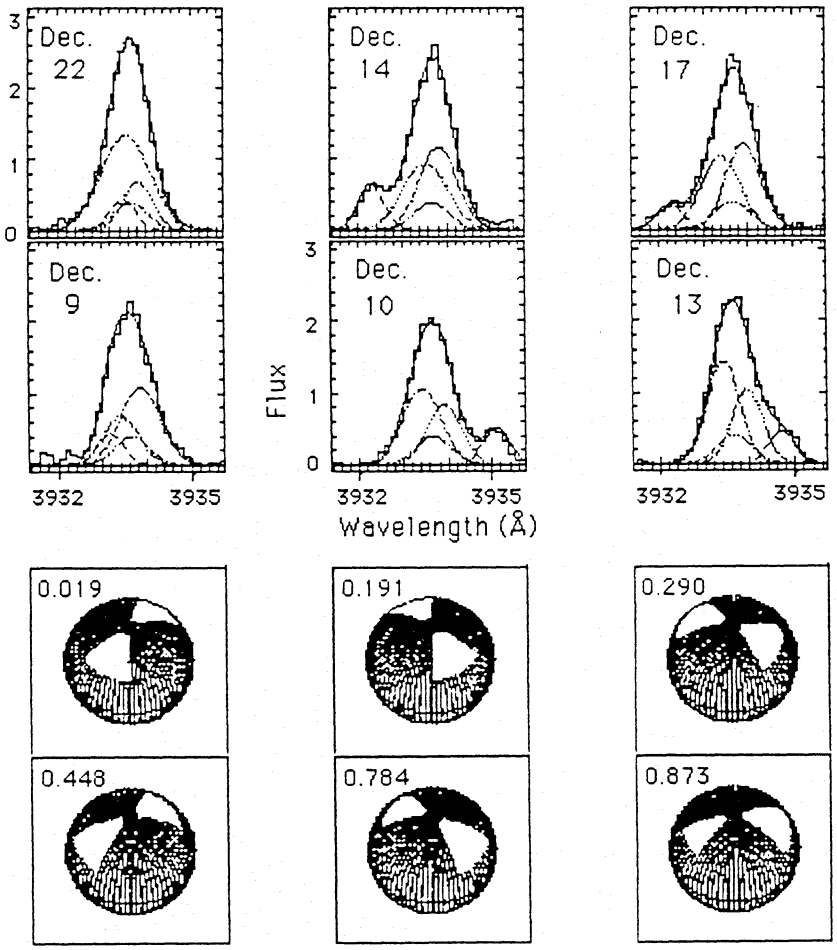

Fig. 4. Observations with the special IAP/IAS spectrometer of the Ca II K spectroscopic modulation. These are residual spectra after the photospheric contribution from the two stars and the Ca II chromospheric emission of the little active secondary have been subtracted. The residual spectra at the different phases have been adjusted with Gaussian components representing the uniform emission centred at nominal orbital velocity, and Doppler-shifted plage components. A preliminary model for the position of plages (Char 1992; Char et al. 1993) is given for illustration and comparison with other surface structures and flaring areas during the MUSICOS campaign. The position is obtained from the differential velocity curve of the two emission components required to account for significant and variable asymmetries on the primary profile

of plages, and are useful for measuring their corresponding velocities and distinguishing different velocity components. Figure 4 shows examples of these Ca II K spectra at a few phases. A method of Ca II spectral imaging (Char & Foing 1993), has been applied to this series to constrain the distribution of chromospheric plages. A similar method was used by Neff et al. (1988) on Mg II IUE data (with somewhat lower S/N = 20). A preliminary adjustment of the spectra is given here for illustration.

An analysis of the Ca II H broad wings led to estimate the cool/hot star contributions and was matched using comparison quiet star profiles that could be subtracted for each phase, providing residual spectra of the chromospheric emission. Fourteen Ca II K residual spectra were used in this analysis. Thanks to the 3 pixel sampling over the spectral resolution (30 km s^{-1}) and signal/noise near 50, it was possible to measure centroid velocities with a precision of 1 km s^{-1} and to resolve the emission into 2 Gaussian active emission components. Velocities for the Gaussian emission components (requiring Wilson-Bappu values for the line widths) could be measured with 5 km s^{-1} rms precision. Velocity curves for the components as well as flux modulation for the fourteen spectra were found to be consistent with two active regions crossing at phases 0.08 and 0.58 with latitudes around 55 and 60 degrees, as determined from our Ca II spectral imaging code. The complete analysis, modelling and results are reported in a separate paper (Char 1992; Char et al. 1994). They show that the Ca II line rises gradually during the flare and attains its maximum after the peak of continuum emission. Also, an excess of Ca II K emission occurred on 18 and 21 December, one and two rotations after the 15 December flare, which is consistent with the post-flare emergence of the hot spot and higher activity indicated by the photometric modelling.

7. The visible flare of 14 December, 15:00 UT

7.1. Photometric observations

In addition to the migrating distortion wave, a flare event was detected from Xinglong near the minimum brightness phase. The amplitudes are 0.18, 0.27 and 0.61 mag in the V, B, and U bands respectively. Figure 5 presents the detailed photometric evolution of this flare. The rise time of the large event at 15:00 UT from half to peak flux is 20 min. A precursor event at 13:30 UT with 0.03, 0.02, 0.05 amplitude over the quiet level respectively in V, B, U can be measured. The observed total duration of the event was 4.5 hours. The photometric precision is equivalent to 0.2% RMS in V and 0.3% in U, which allows us to assess the reality of temporal substructures during the flare. The light curves indicate, in all three channels with different

© European Southern Observatory • Provided by the NASA Astrophysics Data System

1994A&A...292..543F

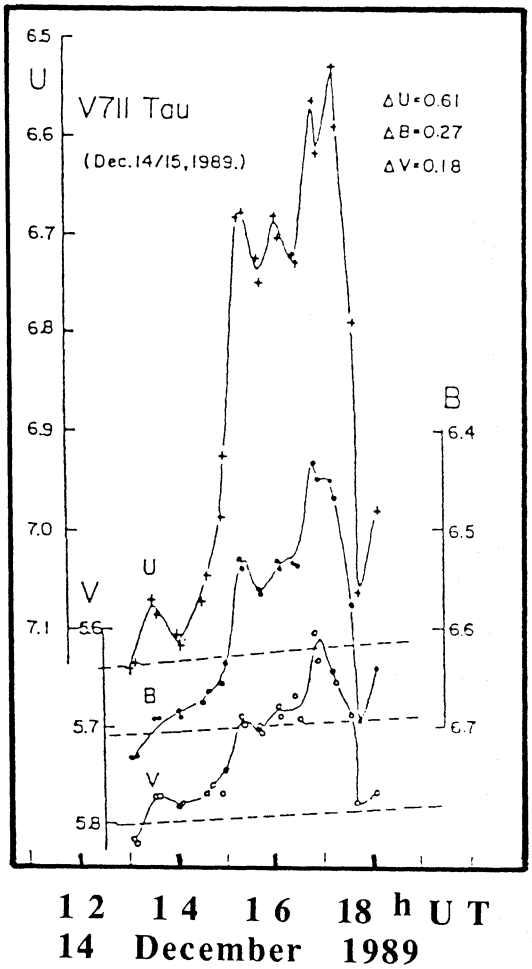

Fig. 5. UBV Photometry of the optical flare of V711 Tau on Dec. 14, 1989 observed at Xinglong. The photometry gives an excess up to 0.61 in U, 0.27 in B and 0.18 in V for this first detected white-light flare on HR 1099. The event seems to be composed of a precursor near 13:00 UT and of a large radiation release lasting at least 2h30 after 14:00 UT. The sudden drop of the flare excess emissions at 17:00 UT is interpreted as the disappearance of the flaring area from view, allowing independent estimate of the flaring position and extent

relative amplitudes, a sequence of 4 or 5 events during this exceptional flaring episode. The last decay phase of the event is remarkably fast. This corresponds to a time scale of only 50 min from maximum to minimum. The apparent extremely fast decay observed after 17:30 could be interpreted in five ways:

(a) An instrumental error affecting the efficiency or the passage of clouds could reduce the flux received by the 3 channels and lead to the expected quiet level. However the relative amplitude reduction is different for the 3 channels so that absorption by grey clouds is highly unlikely.

(b) The last two data points could be very noisy but this noise would have to be significantly larger than the error bar consistent with previously observed dispersion.

(c) An intrinsic very fast decay of the flare signal on 20 min time scale

(d) The flare could in principle be occulted by the companion star, but then the time scale would be shorter than observed or that would require the kernel of white-light emission to be located far above the stellar surface. This is unlikely as the stellar photospheres are well separated in this non-eclipsing system and the flare plasma seems to be localised near the primary as inferred from Hα and photospheric line velocity information.

(e) The occultation of the flaring area could be due to the stellar rotation. A flare structure of longitude extent ΔL would be occulted by the limb during a time interval $t = \Delta L \times \text{Period}/2\pi$. In support of this interpretation, we must note that the phase of the sudden flare decrease (phase 0.46) corresponds well to the phase when the large spot complex ('cool spot 2') is at the limb and is partially occulted by the limb for its lower latitude parts. For a total disappearance time of 50 min this would correspond to a longitude extent $\Delta L = 2\pi/80 = 4.5$ degrees, equivalent to 212 Mm $\times \cos B$ (where B is the latitude) on the star. This is smaller than the diameter derived for the photometric spots from the light curve modelling, but we expect that the flare kernels are significantly less extended that the overall spot area as it is the case on the Sun.

The last data point of the measurements shows a flux level still indicative of continuing flaring activity. No photometry obtained immediately after this event from another site is available. We assume explanation (e) in the subsequent analysis.

7.2. Balmer Hβ and Hα observations

The flare was also observed at Xinglong through Hβ narrow/wide filter photometry. The flux increase observed in the narrow and wide band Hβ channels (respectively up to 28% and 20% increase in the narrow and wide Hβ channels) also gives information on the flare emission. The difference between the magnitude variations $\Delta H\beta_N$ through the $\Delta\lambda_N = 37$ Å narrow Hβ filter and $\Delta H\beta_W$ through the 190 Å wide filter allows one to distinguish the pure Hβ line emission equivalent width increase from local continuum variations. Using the centre transmission T_{max} and width $\Delta\lambda$ (FWHM) of each filter, one can derive the measured flux

$$F\text{H}\beta = T_{max} \times F_c \times (\Delta\lambda/2\text{- EW})$$

for a given continuum flux F_c and line equivalent width EW. The factor 1/2 comes from the integral of the transmission over the filter being $\Delta\lambda^* T_{max}/2$ while the transmission is T_{max} at the Hβ line position). Thus the line equivalent width variation can be obtained from the measured magnitude variation in each channel:

$$\Delta\text{EW} = (1 - 10^{(\Delta H\beta_N - \Delta H\beta_W)/2.5})\Delta\lambda_N/2$$
$$= -1.4\,\text{Å (at flare maximum).}$$

This corresponds to an increase in the flux of the Hβ line, which is already in emission in the preflare state.

The spectrograms obtained simultaneously at Xinglong show an increase of the Hα equivalent width from 3.14 to 4.04 Å at the beginning of the flare (from 14:00 to 15:00 UT). Our calibration of the near Hα continuum of 32 10^{-12} erg cm^{-2} Å^{-1} s^{-1},

© European Southern Observatory • Provided by the NASA Astrophysics Data System

1994A&A...292..543F

derived from the R magnitude 5.25, gives an emission Hα flux of 95 10^{-12} erg cm^{-2} s^{-1} at the beginning of the flare at 14:44 UT rising to 150 10^{-12} erg cm^{-2} s^{-1} at 15:57 UT. The Hα rise seems to precede smoothly the optical flare by 30 min, and then evolves and decay more gradually than the optical flare. The flux and the velocity variations of the Hα flare indicate that the flare plasma followed the orbital motion of the primary star, and thus is perhaps linked to a magnetic structure on this star. Even after the white-light flare had suddenly stopped likely due to the photospheric flare area moving out of view, Hα spectra obtained at Catania observatory 4.5 hours after the flare maximum showed a significant excess consistent with the decay phase, indicating that the Hα emission originated at large height and was only partly occulted at this time.

7.3. Flare radiative losses

Let m_0 be the apparent magnitude of the system outside flares at a given colour, and m be the observed magnitude during the flare. Thus the equivalent intrinsic magnitude m_F of the flare component taken alone (with flux $f_F = f - f_0$) is given as a function of the observed magnitude variations $m - m_0$ for any colour:

$$m_F - m_0 = -2.5\log(f/f_0 - 1)$$
$$= -2.5\log[10^{-0.4(m-m_0)} - 1] .$$

One can thus deduce the intrinsic equivalent magnitude and colours of the flare component as a function of the observed magnitude variations. For the observed enhancements at flare maximum $\Delta V = -0.18$, $\Delta B = -0.27$ and $\Delta U = -0.61$, and preflare values $V_0 = 5.71$, $B_0 = 6.63$ and $U_0 = 7.09$, we find that the intrinsic magnitudes and colours for the flare taken alone are $V_F = 7.56$, $B_F - V_F = 0.433$ and $U_F - B_F = -0.606$. The flare flux outside Earth can be obtained from the relation $\log(f_{V_F}) = -0.4V - 8.43$ (Allen 1973) and other relations for f_{B_F} and f_{U_F}, where the fluxes f are expressed in erg cm^{-2} Å^{-1} s^{-1}. This gives flare fluxes of $f_{V_F} = 3.52\,10^{-12}$, $f_{B_F} = 4.29\,10^{-12}$ and $f_{U_F} = 4.5\,10^{-12}$, while the preflare fluxes are $f_{V_0} = 19.3\,10^{-12}$, $f_{B_0} = 15.1\,10^{-12}$ and $f_{U_0} = 6.82\,10^{-12}$. We interpret the excess ultraviolet flux $U_F - B_F = -0.606$ for a stellar atmosphere with colour $B_F - V_F = 0.433$, as the signature of Balmer emission lines and Balmer continuum enhancement (see below). The Hβ fluxes can also be estimated at peak from the continuum flux and the derived equivalent width -1.4 Å (negative EW means emission) giving: $f_{H\beta} = f_{cont}\Delta EW = 27\,10^{-12}$ erg cm^{-2} s^{-1}. Integrated over the flare duration and at 36 pc distance, this corresponds to Hβ losses of $4\,10^{34}$ erg, while Hα losses are $6.5\,10^{34}$ erg.

7.4. Flare projected area, position and height of Balmer line emission

The $B - V$ colour of the flare at maximum could be interpreted as an effective temperature of 6580 K (Allen 1973), equivalent to a spectral type F4.4. However the $U_F - B_F$ colour is extremely blue (for this spectral type it is normally -0.01), indicating an ultraviolet excess near 3700 Å. A star of spectral type F4.4 would correspond to an absolute magnitude $V_{ref} = 3.69$ and a radius of 1.22 solar radii. One can derive an equivalent area A_{eq} of the flare, based on the measured V_F and $B_F - V_F$ magnitudes and assuming a distance d of 36.2 pc for HR 1099. The expression $V_F - V_{ref} + 5 - 5\log d = -2.5\log A/\pi R^2$ gives $A_{eq} = 8.5\,10^{21}$ cm^2 $= 0.55\pi R_0^2$. This gives a surface coverage at flare maximum of 3.6% of the visible projected primary surface taking for the primary a radius of 3.9 $R_\odot$.

For this flare area, and a flare longitude extent $\Delta L = 2\pi/80$ determined from the occultation time of 50 min, this would correspond (for an equatorial structure) to a latitude extent $\Delta l = 4 \times 2\pi/100$, about 25% of the stellar radius. We conclude that the flare may be elongated along the limb (similar to solar-type limb flare ribbons). We take into account that the foreshortening angle to the normal θ depends on the pole inclination and to the flare position. The physical flare area A must be corrected for a foreshortening effect in $\cos\theta$ and a centre-to-limb brightening of flares by $1 - \varepsilon + \varepsilon\cos\theta$ with ε about -2 (Machado et al. 1980; Houdebine 1992); thus $A_{eq} = \int \delta A(1 - \varepsilon + \varepsilon\cos\theta)\cos\theta$. Based on the lag between the flare maximum and its occultation, and assuming a latitude of 30 deg., consistent with Zhai et al. (1994) average hot spot position, we calculate a value of $\cos\theta = 0.18$ at the flare maximum when the previous projected area was determined. This also explains why the flare appears specially elongated along the limb due to the strong foreshortening at these low values of $\cos\theta$ (in particular below 0.2). This indicates that the physical area is about 2.1 times higher than A_{eq}. Taking this into account, we derive for the white-light flare a physical area of $1.8\,10^{22}$ cm^2. The deduced flare area would correspond to only the receding part of the combined hot spot 1 ($0.51\,10^{22}$ cm^2) and cool spot 2 ($3.14\,10^{22}$ cm^2) derived from the photometric modelling (Zhai et al. 1994), when taking into consideration the estimated areas, phase and the observed occultation.

From the time delay of 3.6 hours (equivalent to 0.052 in phase) between the Balmer partial occultation compared to the white-light total occultation, one may derive information on the height of the Balmer line emitting structure. For assumed flare latitudes $B = 0$, 30 and 45 degrees, we derive a height of respectively 0.029, 0.022, 0.010 (expressed in fraction of stellar radius) or of 80, 60 and 29 Mm. However the Balmer line emission height may represent only the low-altitude low-temperature part of large magnetic loops which can reach far into the corona.

8. The visible flare of 15 December, 1:00 UT

8.1. Time variations of the Hα flux during the MUSICOS campaign

Considering available Hα spectrograms from the different sites, we have derived the time evolution of the Hα equivalent widths over the 4 days of observations (Fig. 6). It appears clearly that

© European Southern Observatory • Provided by the NASA Astrophysics Data System

1994A&A...292..543F

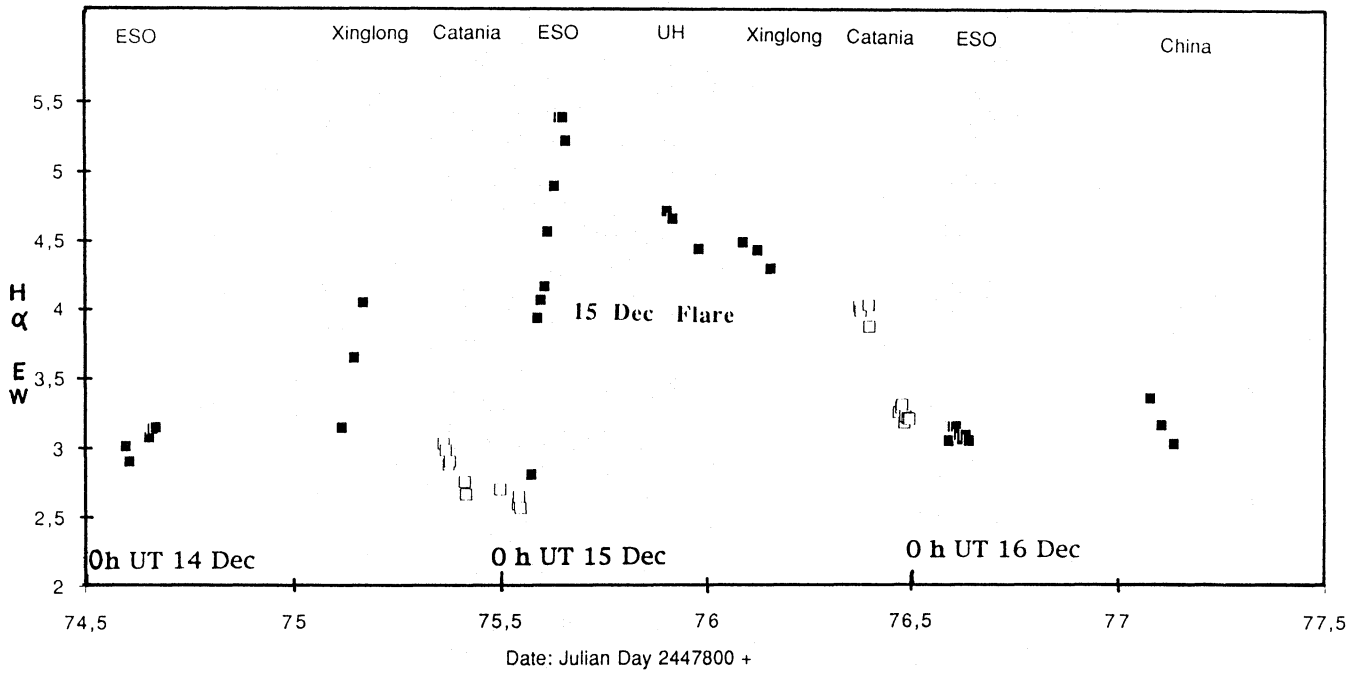

Fig. 6. Variation of Hα equivalent widths during the MUSICOS campaign. The series shows the Hα counterpart of the 14 Dec., 15:00 UT white-light flare observed at Xinglong, with the decay observed from Catania. The second white-light flare of 15 Dec., 1:00 UT is then observed at ESO with the decay phase covered from Hawaii, Xinglong and Catania. The following ESO spectra on 16 Dec. do not show sign of variability, suggesting that the flaring area is then out of view

a second optical flare had already started at 2:00 UT on 15 December. ESO 1m Ca spectrophotometer observations showed in fact a significant enhancement in the adjacent blue continuum as early as 1:10–1:40 UT. Hα variations could be followed later from the ESO, Hawaii, China and Catania sites. This is the second convincing optical flare ever reported on HR 1099, the first one being the one detected from Xinglong and Catania some 12 hours before!

The flare showed a typical Hα EW increase of 2.2 Å between the first spectrum at 1:46 UT and the Hα maximum at 3:20 UT. The Hα rise time (from 1/4 to 3/4 of maximum) was 50 min, and the rise was rather linear in time from the second flare spectrum to the maximum. The first Hα spectrum at 1:46–2:06 UT of the ESO series is already affected by flare (as compared to preflare Hα level measured at Catania just before). For the Hα flare spectra, we estimated the effect due to the fast enhancement (up to 35% at flare continuum maximum) of the surrounding continuum around 6563 Å which affects the EW (even for a fixed Hα emission). As we do not have $UBV(RI)c$ photometry before 3:00 UT, we estimated the enhanced R magnitude by the relation found between R and the equivalent 3950 Å flux during the decay phase of the flare. Taking this effect into account, and a synthetic R flux light curve, we estimate that the Hα emission line flux increased from 95 10^{-12} erg cm^{-2} s^{-1} before the flare with a similar rise time to the continuum, and reached a plateau of 250 10^{-12} erg cm^{-2} s^{-1} after 2:20 UT until the end of the ESO Hα measurements at 3:40 UT.

The flare decay was followed from the other sites at Hawaii and Xinglong, and the e-folding decay time for the Hα flare was approximately 22 hours. On the following observing night at ESO, the Hα equivalent width remained remarkably low and constant at a level of 3.08 $\pm$0.048 Å. The low quiet level of Hα emission attained on 16 December was very similar to that observed on 14 December, with no signature of a flare.

8.2. Photometry and energy budget of the flare

First, the Ca K IAP/IAS special spectrometer detected an enhancement of the 3934 Å continuum near the Ca K line (Fig. 8) that can be translated as a 3950 Å continuum flux that increases from 9.5 10^{-12} erg cm^{-2} Å^{-1} s^{-1} at 0:38–1:08 UT, to 17.9 10^{-12} at 1:10–1:40 UT, and to 33.7 10^{-12} units at 1:45–2:15 UT. Unfortunately, the series of Ca K measurements was stopped at that time. The last data points of this flare correspond to an increase at 3950 Å, which is 4.9 times the peak value of the flare observed at Xinglong the previous day. Immediately thereafter, photometric measurements were obtained in the Cousins $UBV(RI)c$ system by the ESO 50 cm photometer during the decay part of this flare (Fig. 7) after 3:00 UT, 2 hours after the start of the flare and 1 hour after the peak of the continuum around Ca K. Still the observed increase in V was 0.55 mag. Following the method described for the analysis of the white-light flare observed at Xinglong, we can estimate the flare fluxes. At the start of the ESO 50 cm photometry, we find flare excess fluxes of f_{V_F} = 13.4 10^{-12}, f_{B_F} = 20.4 10^{-12}, and f_{U_F} = 30 10^{-12} erg cm^{-2} Å^{-1} s^{-1}, while the preflare fluxes are f_{V_0} = 19.3 10^{-12}, f_{B_0} = 15.1 10^{-12}, and f_{U_0} = 6.82 10^{-12} erg cm^{-2} Å^{-1} s^{-1}. The estimated radiated

© European Southern Observatory • Provided by the NASA Astrophysics Data System

1994A&A...292..543F

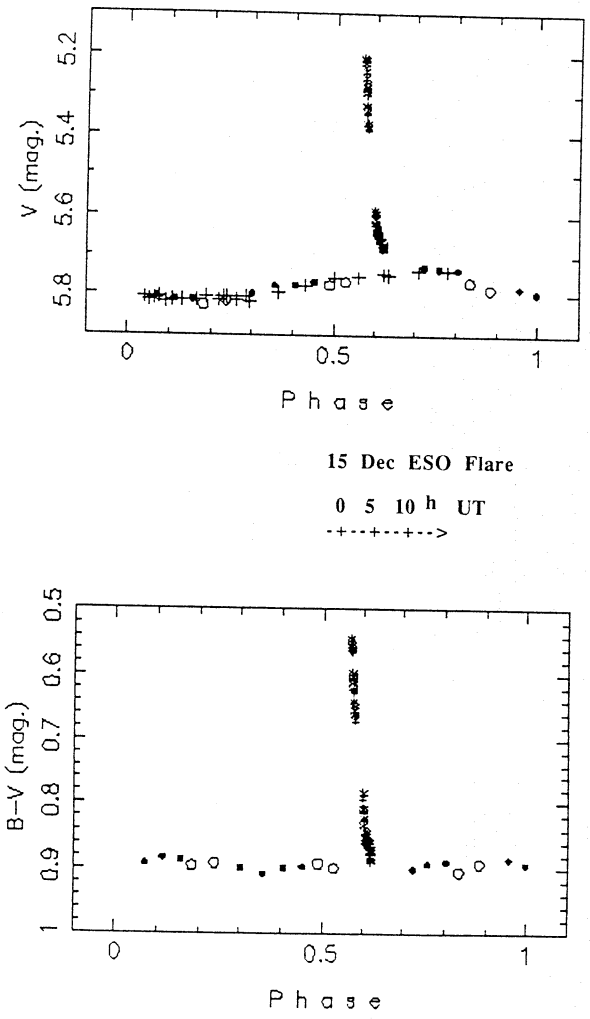

Fig. 7. Photometric variations observed during the 15 December flare at the ESO 50 cm telescope (stars) compared to the rotational modulation light curve out of flare (points and circles). The flare was covered photometrically starting after 3:00 UT, about 2 hours after the impulsive start of the flare. The broad band photometry still indicates an excess of 0.55 magnitude in V at 3:00 UT and an $1/e$ decay time of 100 min. The integrated colour of HR 1099 during the flare becomes bluer than $B-V = 0.54$. This allows one to estimate over 10^{38} ergs released in the measured photometry during this giant flare

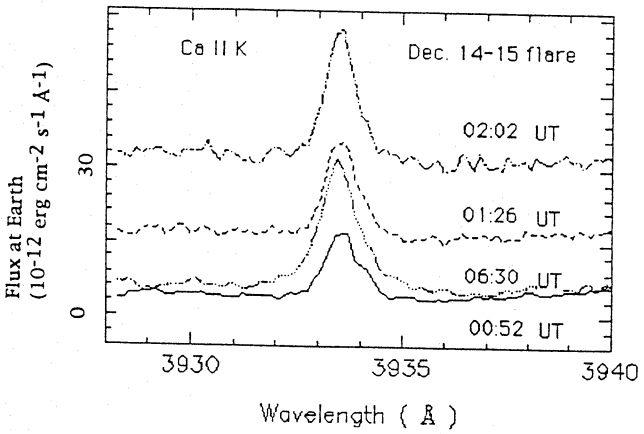

Fig. 8. Four spectra of HR 1099 on December 15 including the Ca II K line taken with the special IAP/IAS spectrometer showing the enhancement of the continuum during the optical flare after 0:52 UT. The solid line represents the preflare spectrum with a flux level similar to previous reference spectra at a similar phase. One sees the impulsive nature of the continuum variations with a typical rise time of 30 min, while the Ca II line variations are more gradual and appear to peak after 2 hours from the start of the flare

power between 3100 and 5900 Å is $8.5\ 10^{33}$ erg s^{-1}. Combining the Ca K continuum measurements and the photometry, we can deduce that the real flare peak occurred between 2h and 2h 20 UT with a peak power of $14\ 10^{33}$ erg s^{-1} in this wavelength interval. The time relation between the different fluxes derived from the flare measurements will be discussed in Sect. 10.1, and is summarised in Fig. 15 for clarity.

Following the method described in Sect. 7 for the Xinglong flare photometry, we derive equivalent magnitudes for the flare component. At the start of ESO observations, we derive intrinsic magnitudes and colours for the flare alone of $V_F = 6.19$, $B_F - V_F = 0.16$, and $U_F - B_F = -0.65$. This flare was significantly bluer than the Xinglong flare (for which $B_F - V_F = 0.43$). A star of spectral type A5, with an effective temperature 8100 K, would have the same $B-V$, an absolute magnitude $V_{ref} = 2.0$, and a radius of 1.78 solar radii. This allows us to calculate an equivalent area for the flare of $A'_{eq} = 13.3\ 10^{21}$ cm^2. However, we expect the flare to occur near the approaching limb. The observed velocities are consistent with this flare being located near the position of the hot spot 1 derived from the photometric solution, which corresponds at this phase to a projection angle $\cos\theta = 0.3$. Taking into account center-to-limb brightening and foreshortening $(1 - \varepsilon + \varepsilon \cos\theta)\cos\theta$, with $\varepsilon = -2$ as before, we derive a physical area 1.39 larger than A'_{eq}, or $1.85\ 10^{22}$ cm^2. This is the same as the physical area derived for the Xinglong flare though observed at a different phase and projection angle. This reinforces our findings that both flares are related to the photometric hot spot.

8.3. *Hα spectroscopy and flows during the flare*

Figure 9 shows the temporal variation of the 10 min Hα spectra observed from ESO, from which we have subtracted the preflare spectrum. Notice the change in the line intensity during the flare. The Hα profile at the start of the flare at 2:04 UT has a FWHM width of 2.7 Å (equivalent to 123 km s^{-1}) and excess blue wing flux in the range 2.2–10.2 Å (corresponding to velocities 100–470 km s^{-1}) that persists from 2:04 to 3:00 UT. The spectrum at 3:00 UT shows a sudden symmetrical broadening of 5.23 Å (240 km s^{-1}). Later spectra, which correspond to the maximum Hα emission, show a red excess extending until 6.2 Å (280 km s^{-1}), with a persistent narrow absorption feature during the three last exposures redshifted from 1.13–1.94 Å (50–90 km s^{-1}). The Hα flux was measured across both impulsive and gradual phases of the continuum flare, peaking about 40–60 min later than the photometry. The total radiative loss in this line was $35\ 10^{34}$ ergs, integrated over this huge Hα

© European Southern Observatory • Provided by the NASA Astrophysics Data System

1994A&A...292..543F

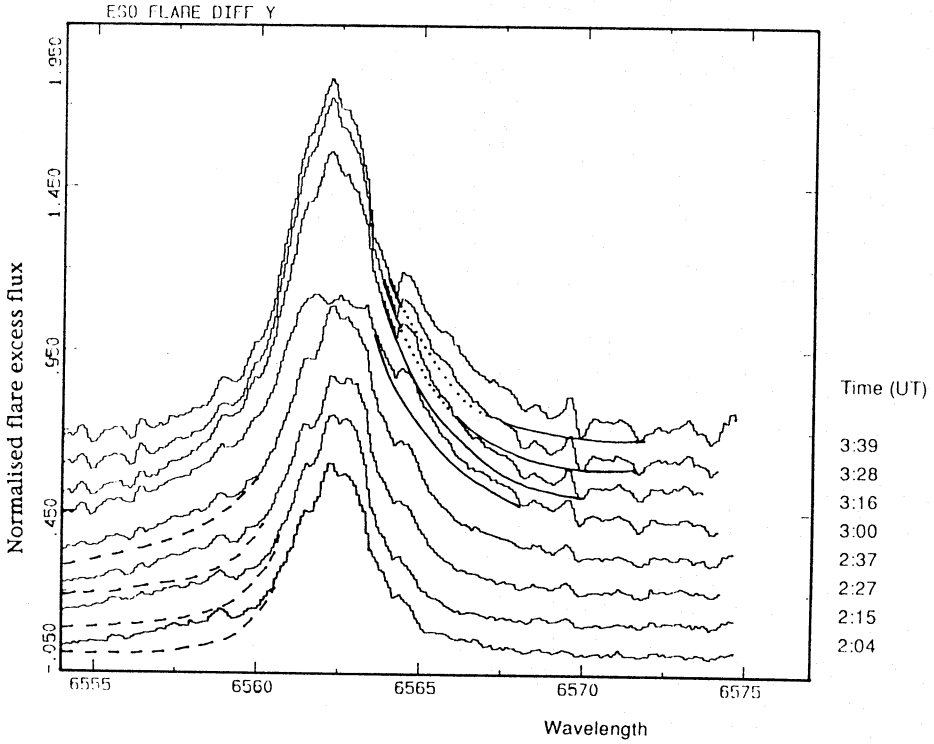

Fig. 9. Time resolved Hα spectra (dynamic spectrum) of the second large optical flare observed on 15 December at ESO. Spectra were taken with 10 min exposures from 1:50, about 40 min after the start of the flare . The first Hα spectrum that corresponds to the smallest equivalent width has been subtracted from the following spectra taken from 2:04 UT to 3:39 UT. The line profile wings has been folded (solid and dashed lines) to show the early excess blue wing and later red excess. The first 4 difference spectra show that with increasing flux, there is excess Hα blue wing emission. The 5th spectrum at 3:00 UT shows a sudden broadening (suggesting turbulent motions) and corresponds to the start of an even faster increase of the flux, with appearance of a red excess emission wing extending to 15 Å. Also visible is a developing redshifted absorption feature in the range 200–300 km s^{-1} from line centre that we interpret as the signature of a system of condensing post flare loops

flare that lasted about 24 hours. Again we could estimate a very large ratio of more than 340 for optical emission/ Hα or of 120 for optical over all Balmer emission for this flare, while values of 40 and 10 respectively are normally encountered in flare stars, consistent with the flare occurring at the limb, increasing the observed continua, but with little effect on Balmer line emission (cf. Avrett et al. 1984; Machado et al. 1980; Houdebine 1992).

9. IUE measurements of the giant flare decay phase

9.1. Display and measurement of SWP spectra

For display purposes we merged together the photometrically-linearised large-aperture SWP spectrograms of HR 1099 to illustrate the appearance of the SWP-LO spectra as well as the temporal development of the post-flare decay on December 16. Figure 10 shows the result. The H I Ly α feature is overexposed in all of the observations. The decline of the emission spectrum – particularly C II λ 1335, C IV λ 1549, and He II λ 1640 – is clearly evident; there even is an obvious fading of the 1700–1900 Å continuum emission.

Although we extracted each of the double exposures into a single spectrum, the temporal information is essential to an understanding of the post-flare cooling phase. Therefore, we extracted spatial cross-dispersion profiles of the double-spectra by adding along the dispersion the uncalibrated fluxes of two

Table 4. Time-resolved fluxes of SWP-LO spectra

Cam. image No.	Obs. start time (UT) (offset ref. pts.)	Relative fluxes (10^{-12} erg cm^{-2} s^{-1}) low-ex	high-ex
(1)	(2)	(3)	(4)
1989 DOY 350 (Dec. 16 post-flare)			
SWP 37828	04:41 (B)	6.14± 0.08	14.3± 0.1
	05:08 (A)	6.14± 0.08	13.4± 0.1
SWP 37829	06:35 (A)	5.93± 0.06	12.7± 0.1
	07:06 (B)	5.37± 0.06	10.3± 0.1
SWP 37830	08:29 (C)	5.36± 0.06	11.9± 0.2
1989 DOY 351 (Dec. 17 post-flare)			
SWP 37834	04:21 (B)	3.99± 0.07	8.44± 0.08
	04:45 (C)	3.59± 0.07	8.20± 0.08
SWP 37835	06:09 (A)	3.49± 0.03	8.19± 0.06
	06:32 (B)	3.33± 0.03	7.37± 0.06

Notes: Col. (3): see col. (3) of Table 3, Col. (4): "low-ex"= sum of O I λ1305, C I λ1657 & Si II λ1815; "high-ex"= sum of C II λ1335, He II λ1640, Si IV λ1400 & C IV λ1549.

© European Southern Observatory • Provided by the NASA Astrophysics Data System

1994A&A...292..543F

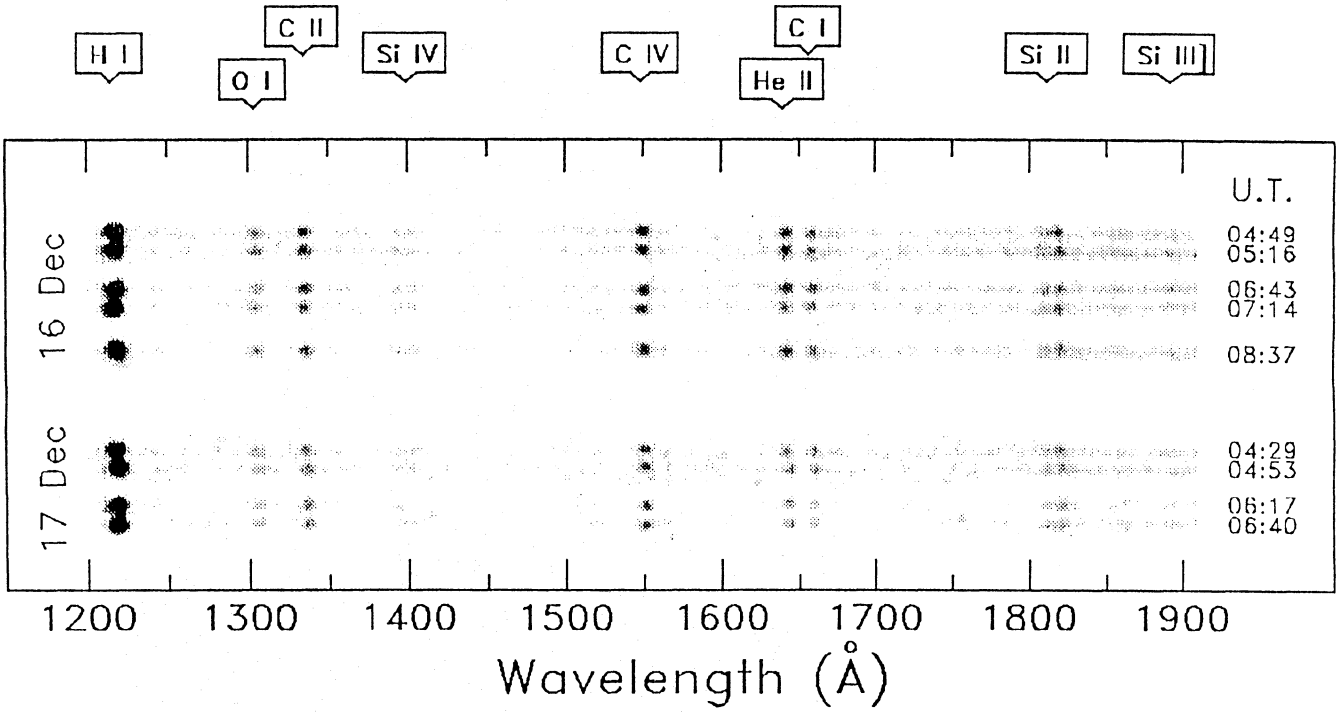

Fig. 10. The IUE SWP low-dispersion spectra obtained during the second large optical flare of the MUSICOS campaign, and a day later during a more quiescent period. The upper two and lower two spectra are double exposures in the large aperture; the middle spectrum is a single exposure. The images are arranged from top to bottom in order of increasing time. They have been photometrically-corrected using a new procedure, and individually background-corrected. All of the images are scaled in the same way (to emphasise the C II and C IV emissions). Note that H I Ly α is heavily overexposed in all of the spectra

groups of emissions: a low-excitation class representing chromospheric conditions ($T < 10^4$ K); and a high-excitation class representing conditions in the subcoronal "transition zone" ($3\,10^4$ K–10^5 K). The derived cross-dispersion profiles are illustrated in Fig. 11. We fitted the spatial profiles using blended least-squares Gaussians; the results are listed in Table 4.

The individual SWP extracted spectra, and the line and continuum fits, are compared in Fig. 12. The differences between each spectrum and the final observation on December 17 (SWP 37835) are shaded to illustrate the significant decline over the first few hours of the post-flare phase. Table 5 summarises the fluxes of the important emissions and a 50 Å band in the far-UV continuum (centred at 1900 Å).

The HR 1099 spectra are quite well-exposed, and the S/N per pixel can reach upwards of 30 in such images. Because the extracted spectrum averages over several pixels in the cross-dispersion direction, and the line-fitting also averages over several samples in the spectral direction, the S/N of a line flux measurement due to the random photometric contribution can be several times higher than the peak S/N at the pixel level. The major systematic error would come through the absolute calibration and could be as much as $\pm 10\%$; however that error is not applicable when comparing the relative behaviour of the same line over a period of time.

9.2. Display and measurement of LWP spectra

The long wavelength IUE echelle spectroscopy presented more of a challenge to analyse than the comparatively simple SWP low-dispersion images. The essential advantage of the LWP spectra – and the source of much of the difficulty – is the velocity discrimination and profile shape information available with the high-dispersion format. An initial attempt to phase the Mg II profiles using the historical ephemeris of Bopp & Fekel (1976, BF) proved to be disappointing. Because small errors in the period can easily accumulate to significant phase shifts when an old ephemeris is used a few thousand orbits later, we derived a current-epoch time-of-conjunction (Time of Conjunction TOC: more massive star in front) from the IUE spectroscopy itself. An accurate ephemeris is essential to Doppler-imaging work.

We utilised the Mg I feature as a velocity fiducial because the broad damping wings – and the associated absorption structure – is dominated by the warmer secondary, while the central emission core is mostly from the cooler primary. We established the velocity of the G-star in each spectrum by cross-correlating the far wings of Mg I at 2852 Å against a template constructed from a variety of G dwarfs for which good-quality LWP spectra were available in the IUE archives. We then separately measured the velocity of the K star by fitting a Gaussian to the Mg I emission core. The relative velocity displacement between the two components depends sensitively on the orbital phase. We compared the orbital phases "predicted" by the measured velocity differ-

© European Southern Observatory • Provided by the NASA Astrophysics Data System

1994A&A...292..543F

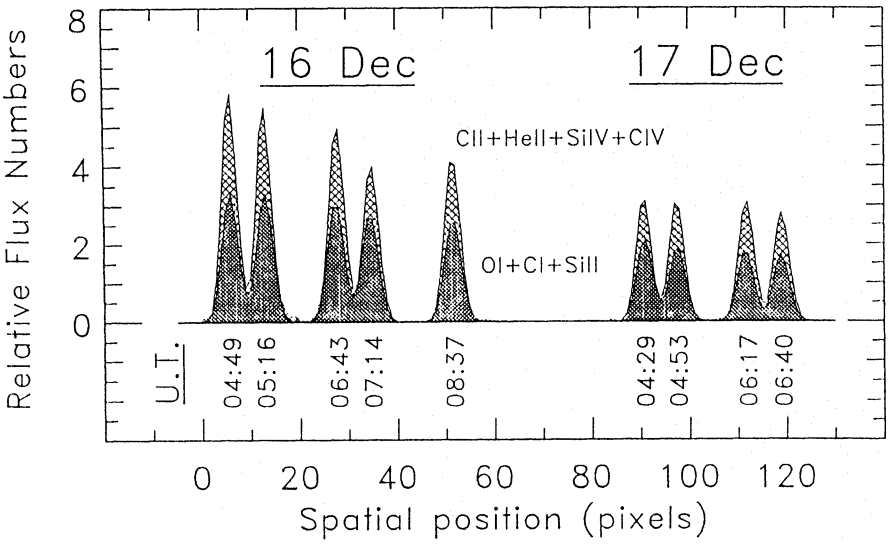

Fig. 11. Cross-cuts of the merged image illustrated in the previous figure. The profiles were determined by adding the fluxes along lines of constant wavelength in the immediate vicinities of two groups of reference features as indicated in the figure: low-excitation, chromospheric emissions (heavy shading); and high-excitation, transition-zone emissions (lighter shading). The decay of the flare appears to be somewhat more rapid in the high-excitation species. By the second day, the emission levels had returned to normal values

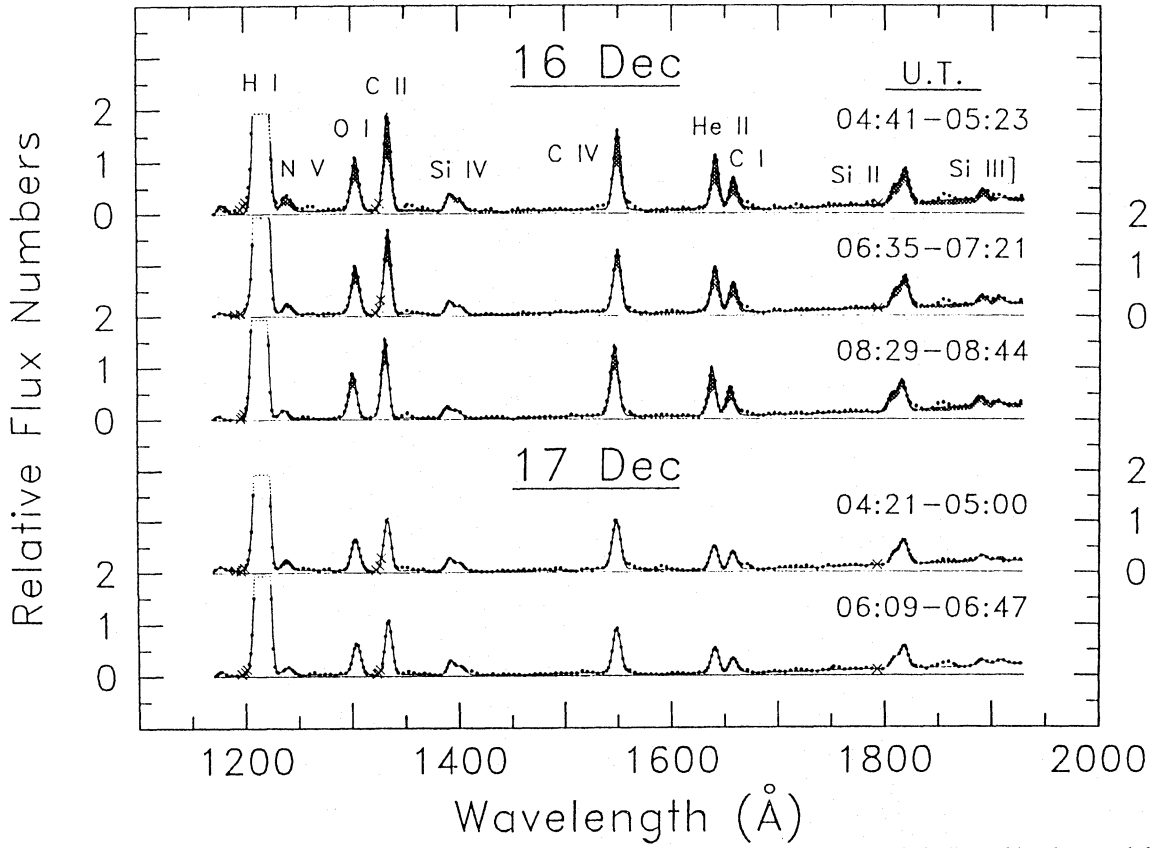

Fig. 12. Extracted spectra of the five SWP low-dispersion exposures. The observed spectrum is indicated by dots, and the numerical fit to it by the solid curves. X's mark portions of the spectra affected by réseau marks: the core of the strong H I Ly α feature is overexposed in all of the observations. The differences between each of the individual spectra and the final one on December 17 are shaded to illustrate the cooling phase of the giant optical flare

ences to those expected from the Bopp & Fekel T_0 and P, to determine whether any significant phase shifts had accumulated. We found that the best-fit to the 1989 December and 1990 February LWP series yielded a phase shift of 0.056 ± 0.011 cycles using the BF period (our TOC occurs $0.056 \times P$ days after that of Bopp & Fekel). Our preliminary TOC is J.D.. 2,447,874.025 which is consistent with Fekel (1983) within 0.5% of the period.

Given the new ephemeris, we compared the predicted and measured absolute velocities of the secondary star (the latter is accurately established by the cross-correlation). Because most of the spectra were offset in the large aperture (wavelengths are

© European Southern Observatory • Provided by the NASA Astrophysics Data System

1994A&A...292..543F

Table 5. Flux of line emissions in the far UV for the different IUE SWP spectra (in 10^{-12} erg cm^{-2} s^{-1})

Line	Wavelength	SWP 37828	SWP 37829	SWP 37830	SWP 37834	SWP 37835
N v	1240	0.84 ± 0.22	0.56 ± 0.06	0.48 ± 0.07	0.57 ± 0.06	0.47 ± 0.08
O i	1305	2.18 ± 0.06	2.05 ± 0.06	1.86 ± 0.08	1.38 ± 0.06	1.26 ± 0.06
C ii	1335	3.79 ± 0.06	3.18 ± 0.08	2.92 ± 0.08	1.95 ± 0.06	2.00 ± 0.06
Si iv	1400	1.26 ± 0.06	1.01 ± 0.06	0.85 ± 0.08	1.00 ± 0.06	1.01 ± 0.06
C iv	1549	5.74 ± 0.12	4.59 ± 0.10	5.30 ± 0.15	3.93 ± 0.09	3.28 ± 0.07
He ii	1640	3.07 ± 0.09	2.71 ± 0.10	2.80 ± 0.14	1.44 ± 0.08	1.49 ± 0.06
C i mult	1657	1.80 ± 0.09	1.73 ± 0.07	1.69 ± 0.08	1.01 ± 0.07	0.87 ± 0.06
Si ii	1815	2.16 ± 0.08	1.87 ± 0.06	1.81 ± 0.06	1.40 ± 0.07	1.28 ± 0.06
Si iii]	1892	0.33 ± 0.12	0.30 ± 0.09	0.37 ± 0.06	0.19 ± 0.08	0.20 ± 0.08
C iii]	1909	< 0.13 (2σ)	0.25 ± 0.07	0.17 ± 0.06	< 0.07 (2σ)	0.19 ± 0.06
continuum	1875–1925	3.09	2.62	2.95	2.37	2.09

Notes: Uncertainties (±1σ) derived from rms deviation of fit from true fluxes; upper limits ("<") are approximately 2σ.

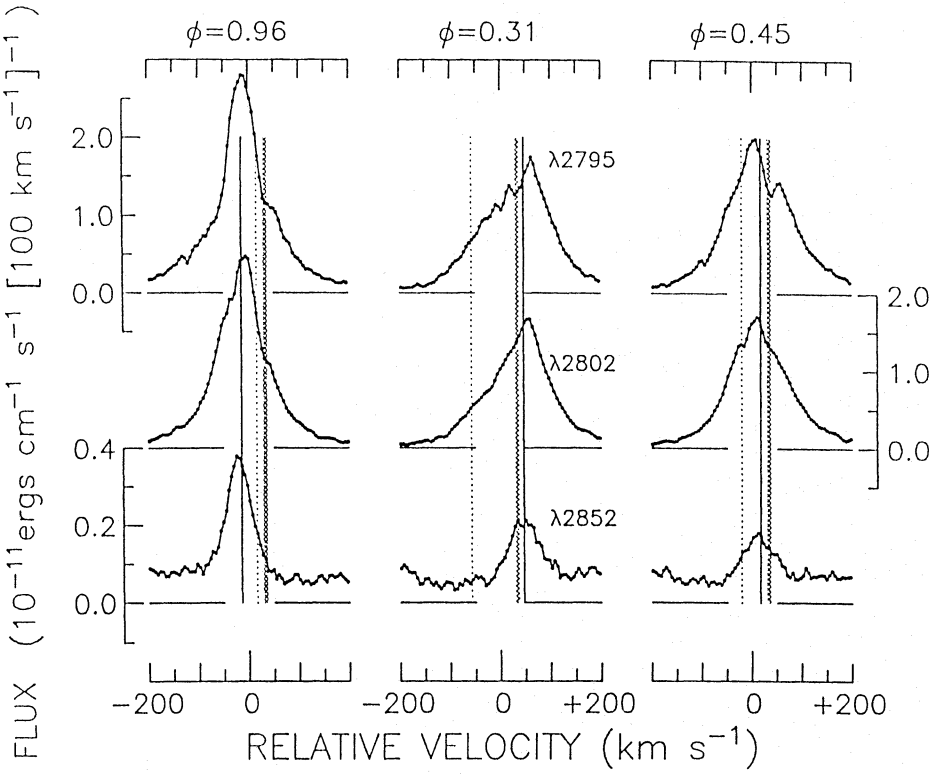

Fig. 13. Co-added spectra of the Mg II and Mg I resonance lines taken during the flare (left panel); one day later (centre panel); and about 50 days later (right panel). The individual spectra obtained during each observing shift, including short offset pseudo-trailed exposures and deep point-source exposures, were difference-filtered in pairs to remove transient defects, and combined in the centre-of-mass reference frame. The velocity of the primary star (K0 IV) at the mean phase of the observation is indicated by the vertical solid line; the velocity of the secondary (G5 V) is indicated by the dotted line; and the predicted velocity of the interstellar absorption components is indicated by the hatched line. The enhancement of the Mg I and Mg II emissions during the 4-hour period of post-flare observations is obvious, compared with the profiles obtained even a day later. The assigned phases are based on a revised ephemeris derived from the IUE spectra of the Mg I wings and emission core

assigned by IUESIPS assuming that the target is perfectly centred), we applied a correction to each wavelength scale based on the nominal displacement of the target from the aperture centre parallel to the dispersion. The standard deviation of the differences was 6 km s^{-1}, comparable to the typical magnitude of the differences themselves and comparable to the positioning errors that one might anticipate given the offset reference points and pseudo-trailing. We then applied the individual differences as additional wavelength corrections (treating them entirely as systematic [e.g., positioning] errors), and coadded the resulting spectra in the reference frame of the system centre-of-mass to produce the three series of merged profiles illustrated in Fig. 13. The spectra of December 16 were obtained close to "first" conjunction (Φ = 0); those of December 17 were obtained shortly after the Φ = 0.25 quadrature (maximum radial velocity separation); and the comparison series taken in early February 1990 were near the second conjunction (Φ = 0.5), essentially opposite in phase to the first series. In all cases distinct absorption features or flux inflections occur in the coadded Mg II h and k emission cores at the predicted velocity of the interstellar medium towards HR 1099 (see, e.g., Ayres & Linsky 1982), adding credence to the assigned velocity scales. The overall enhancement of the Mg I and Mg II emissions on the day of the large optical flare is unmistakable.

Figure 14 shows the individual LWP spectra obtained on December 16 during the post-flare cooling phase. These spectra have been registered to the velocity frame of the K0 primary according to the new ephemeris and the additional corrections

© European Southern Observatory • Provided by the NASA Astrophysics Data System

1994A&A...292..543F

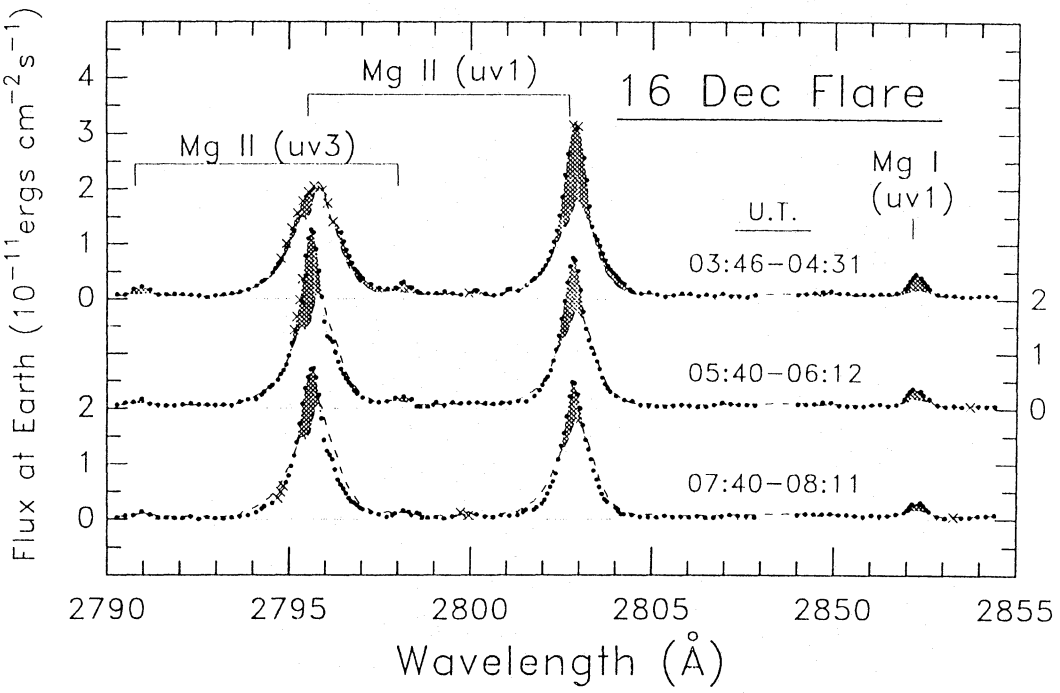

Fig. 14. Individual LWP echelle spectra of the 2800 Å region obtained during the post-flare period on December 16. The dots are the observed spectra; X's indicate points affected by saturation or réseau marks. The first exposure was 45 minutes in duration, which explains the overexposure of the λ2796 core. The two subsequent exposures were 2 × 10 minute pseudo-trails (at opposite ends of the large aperture), and are well-exposed at the *k* line core. The wavelength scales are in the reference frame of the active K0 star. The dashed curves represent the co-added spectrum from 1990 February 3, at the opposite orbital phase to the flare: the emission components of the Mg I and Mg II resonance lines have been *reversed* in velocity to simulate the appearance of the nonflare chromospheres of the primary and secondary at the time of the flare. The differences between the flare profiles and the reference "quiescent" profiles are shaded to illustrate the initial substantial enhancement of the Mg II emission, and its rapid decline, during the post-flare cooling phase

described in the previous section. In order to illustrate the effect of the flare, we shaded the difference between the three flare spectra and the subsequent comparison observation at Φ = 0.45 registered to the primary's frame, but *reversed* in velocity over the extents of the line emission cores. The Φ = 0.45 profile essentially shows the appearance of the other side of the K0 star from that on which the December 16 flare occurred: it is not the ideal comparison, but is the only suitable one available close in time to the flare itself. Notice the enhancements of the uv3 subordinate lines of Mg II in addition to those of the resonance transitions. These enhancements were previously seen in a flare on UX Ari (Simon et al. 1980).

We measured the fluxes of the Mg II uv1 lines in all of the spectra (note the *k* component is overexposed in all of the deep point-source exposures which leads to underestimate the corresponding flux); and the fluxes of Mg I uv1 and Mg II uv3 (where visible) in the deeper exposures. We used direct numerical integrations (of the fluxes between, for example, the k_1 minimum features: see, e.g., Linsky & Ayres [1978]) for the resonance transitions, and least-squares Gaussian fitting for the Mg II uv3 transitions. The results are summarised in Table 6.

10. Discussion

10.1. Temporal variations of radiative losses in continua and Balmer lines

We summarise in Fig. 15 the temporal variations of the main radiative losses during the two large white-light flares. The fluxes were estimated in the photometric bands and in the Balmer lines using conversion parameters as described in Sects. 7 and 8. To allow a proper comparison between continua and Balmer losses, photometric fluxes are integrated over the respective *U*, *B*, *V*, *R* filter bandpasses of 690, 960, 900, 900 Å and expressed thus in erg cm^{-2} s^{-1}. The Balmer line emission is estimated in the same units, using a relation (Butler et al. 1986) Balmer = 11/3 Hα during flares. We used the measured Hα or Hβ equivalent width and the continuum conversion, at the corresponding wavelengths (as in Sects. 7.1 and 8.1). One can note that data derived from simultaneous Hβ filter measurements and Hα spectroscopic measurements are consistent with Hα = 1.6 Hβ. One can also recall the Butler et al. relation giving the soft X-ray flux as 34/3 Hα for various flares.

For the Xinglong flare, integrating the broad band fluxes from 3100 to 5900 Å and taking into account the distance of HR 1099, we find a peak emitted intensity of 1.65 10^{33} erg s^{-1}. The losses in this wavelength range are thus 8 10^{36} erg over the 2h30 flare event. Furthermore, radiative losses in the ultra-

© European Southern Observatory • Provided by the NASA Astrophysics Data System

1994A&A...292..543F

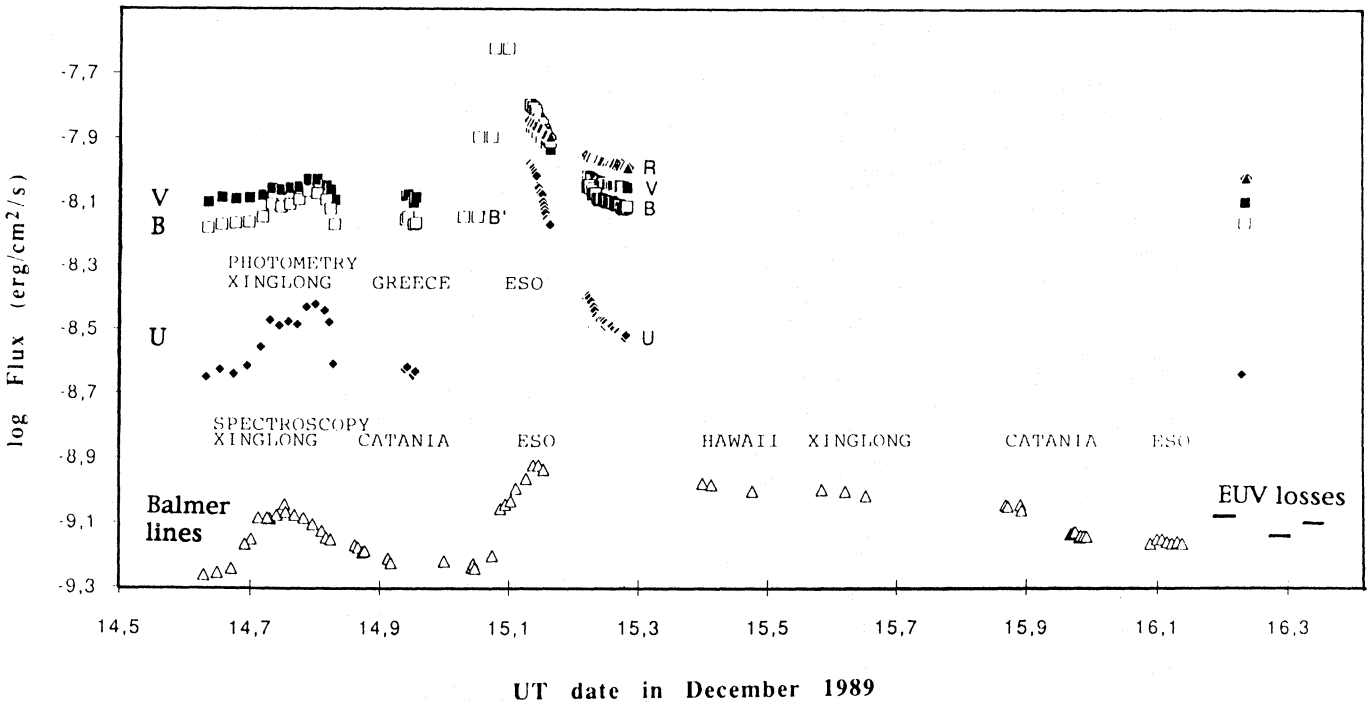

Fig. 15. Temporal variations of the estimated fluxes (in erg cm^{-2} s^{-1}) in the various photometric bands and in the Balmer lines during the two giant white-light flares. The photometric fluxes are integrated over the respective UBVR filter bandpasses of 690, 960, 900 and 900 Å to represent the radiative continuum losses in erg cm^{-2} s^{-1}. The Balmer emission in the same unit is estimated from a relation Balmer line emission = 11/3 Hα. The fluxes measured by IUE in the late post-flare stage on 16.2 December with respective fluxes (in erg cm^{-2} s^{-1}) of 10^{-10} for the Mg II h and k lines, 15 10^{-12} for the high excitation SWP lines and 6 10^{-12} for the low excitation SWP lines. Scaling from EUV emissivities computed by Landini and Monsignori-Fossi (1990), we derive EUV losses of 8.2 10^{-10} erg cm^{-2} s^{-1} at this phase, which are similar to Balmer line losses. The X-ray emission may also be estimated as 34/3 Hα or 3.1 times the Balmer line emission (Butler et al. 1988). The derived continuum and Balmer fluxes indicate a very high optical continuum/Balmer ratio compared to normal flares on dwarf stars, but consistent with the ratio found on limb flares

violet and the near-infrared can be of the same order as this visible radiative loss, and we have no direct information on the X-ray, XUV, UV and IR emission during the flare. The flare flux excess is about 80% stronger in U, and 50% stronger in B than in V. This indicates a significant contribution shortward of 3500 Å, consistent with the derived blue colour of the flare component. From the measurements of the first white-light flare detected at Xinglong, we estimate the Balmer line losses as 11/3 Hα = 24 10^{34} erg (less than 3% of the derived optical losses), and the X-ray losses using the relation (Butler et al. 1986) Lx = 34/3 Hα = 74 10^{34} erg (less than 10% of the optical losses). This indicates that the emission from Balmer lines and soft X-ray emission should be small contributors to the radiative budget. By extrapolating around the observed range, we can give a conservative lower limit to the radiative losses dominated by the continuum radiation of 20 10^{36} ergs. However, the contribution of kinetic energy to the overall flare budget is important as indicated by the flows of several hundreds of km s^{-1} observed in Hα.

For the ESO-detected white-light flare, the losses appear to be dominated by continua in the U and B bands, which are two times stronger than the fluxes in the V and R bands. Again the role of Balmer line and soft-X ray emission seems to be minor in the energy budget for this flare. We have UV observations only in the late post-flare phase, about 25 hours later than the flare peak. The flare excess fluxes measured by IUE on 16.2 December are respectively 10^{-10} erg cm^{-2} s^{-1} for the Mg II h and k lines, 15 10^{-12} erg cm^{-2} s^{-1} for the high excitation SWP lines and 6 10^{-12} erg cm^{-2} s^{-1} for the low excitation SWP lines. We can estimate the total transition region EUV emission at this phase of the flare from the measured C IV line flux, with a scaling factor of 165 using the emissivity calculations of Landini & Monsignori-Fossi (1990). We obtain total EUV losses of 8.25 10^{-10} erg cm^{-2} s^{-1}, about 1.2 times the previously derived Balmer line flare emission, while the X-ray losses were estimated to 3 times this value. Thus the X-ray and EUV losses lines seem to contribute above 15% of the overall energy budget during the late post-flare stage. Considering the continuum half rise time of 40 min and the e decay time of the continuum of 1h 40min, we estimate a radiated energy over the white-light flare equivalent to 1.2 10^{38} erg only for the range 3100–5900 Å. Taking into account losses in the UV, near IR and X-ray, and the kinetic energy could lead to a total energy budget more than twice this value.

We estimated also respectively an equivalent area of 0.89 solar disk units for the "ESO" optical flare, and 0.55 solar disk units for the "Xinglong" flare, but a physical area which is the same for both flares (1.8 10^{22} cm^2 or 1.17 solar disk area) after

© European Southern Observatory • Provided by the NASA Astrophysics Data System

1994A&A...292..543F

Table 6. Measured fluxes of LWP-HI spectra: Mg II (uv1 & uv3) & Mg I (uv1)

Fitting method	Wavelength (Å)	Bandpass (Å)	FWHM (Å)	Flux at Earth (10^{-12} erg cm^{-2} s^{-1})	Cont. flux (10^{-12}cgs Å^{-1})	Bad points (%)
LWP16928H (start 16 December 89, UT 3:45, exposure 45 min)						
Gauss	2790.8		0.58	1.10 ± 0.03	0.51	0
Gauss	2798.0		0.45	0.73 ± 0.05	1.28	0
NumInt	2795.2	4.750		(35.9)	–	33
NumInt	2802.9	4.600		44.7	–	4
NumInt	2852.0	1.450		3.34	–	0
LWP16929H (start 16 December 89, UT 5:40, exposure 2 × 10 min)						
NumInt	2794.9	3.650		34.6	–	6
NumInt	2802.6	4.200		28.3	–	0
NumInt	2851.8	1.450		2.76	–	0
LWP16930H (start 16 December 89, UT 7:39, exposure 2 × 10 min)						
Gauss	2791.3		0.80	0.42 ± 0.02	0.41	0
NumInt	2795.5	4.350		30.0	–	5
NumInt	2802.8	3.450		23.9	–	0
NumInt	2852.3	1.650		2.44	–	0
LWP16931H (start 17 December 89, UT 3:27, exposure 45 min)						
NumInt	2795.8	4.350		(28.7)	–	29
NumInt	2803.0	4.000		24.8	–	0
NumInt	2852.7	1.300		1.96	–	14
LWP16932H (start 17 December 89, UT 5:18, exposure 2 × 10 min)						
NumInt	2795.6	4.450		23.6	–	5
NumInt	2802.7	3.900		20.2	–	0
LWP16933H (start 17 December 89, UT 7:08, exposure 2 × 10 min)						
NumInt	2796.1	3.800		25.6	–	6
NumInt	2803.0	3.450		20.2	–	0
LWP16934H (start 17 December 89, UT 8:12, exposure 36 min)						
Gauss	2790.8		0.55	0.38 ± 0.04	0.51	0
Gauss	2798.2		0.69	0.52 ± 0.03	0.64	0
NumInt	2795.3	4.350		(29.8)	–	7
NumInt	2802.9	3.700		24.5	–	0
NumInt	2852.4	1.550		2.08	–	6
LWP17287H (start 3 February 90, UT 19:45, exposure 2 × 10 min)						
NumInt	2795.5	4.850		30.0	–	4
NumInt	2802.7	4.050		23.0	–	0
LWP17288H (start 3 February 90, UT 20:48, exposure 2 × 10 min)						
NumInt	2795.8	4.150		31.5	–	7
NumInt	2803.1	3.750		23.9	–	0
LWP17289H (start 3 February 90, UT 21:50, exposure 67 min)						
Gauss	2791.0		0.78	0.47 ± 0.01	0.51	0
Gauss	2798.0		0.70	0.55 ± 0.02	0.64	0
NumInt	2795.5	4.400		(25.9)	–	38
NumInt	2802.9	4.100		26.1	–	1
NumInt	2852.2	1.450		1.82	–	0

Notes for Table 6: Col.(1): Gauss= least-squares Gaussian fit. NumInt= direct numerical integration. Col. (2): centre wavelength for numerical integration or derived wavelength from Gaussian fit. Col. (3): bandpass for numerical integration. Col. (4): full width at half maximum intensity derived from Gaussian fit. Col. (5): flux from fit, with uncertainty derived from rms deviation of fit from true fluxes (Gauss, only). Note that the MgIIk fluxes at 2795 Å derived from the deep exposures indicated with () for images LWP-HI 16928, 16931, 16934, 17289 are *underestimated due to saturation.* Col.(6): background 'continuum' flux level in erg cm^{-2} s^{-1} Å^{-1} assumed in fitting procedure. Col. (7): percentage of fitted points affected by saturation or réseau marks. See Table 3 for the catalogue of corresponding observations and exposure centre positions.

© European Southern Observatory • Provided by the NASA Astrophysics Data System

1994A&A...292..543F

correction for limb angle. We find in both flares (see Sects. 7 and 8) a very high optical/Balmer luminosities ratio of more than 110 for optical emission/ Hα for these flares, while a value of 40 is usual for other flares on the Sun and dMe stars. However from the derived limb angles ($\cos\theta = 0.18$ and 0.3 respectively), we expect a strong centre-to-limb brightening by factors of 2.64 and 2.4 respectively (Machado et al. 1980; Avrett et al. 1986; Houdebine 1992) for the optical continua but no significant brightening of the Balmer Hα and Hβ lines, which reconciles better the derived optical/Balmer ratio with other flare observations. The surface intensity can be derived from the observed ones $I = I_{obs}(1 - \varepsilon/3)\cos\theta(1 - \varepsilon + \varepsilon\cos\theta)$ knowing the limb angle and center-to-limb brightening ($\varepsilon = -2$). We find that the optical continuum radiative losses are $2.8\,10^{37}$ and $2.75\,10^{38}$ erg, respectively, for the two flares.

10.2. Estimate of densities from Hα fluxes and profiles

For the Hα peaks of both flares we can derive a surface intensity I from the observed fluxes Φ at Earth, considering the distance of 36 pc, the physical area $A = 1.8\,10^{22}$ cm^2 and the limb angle: $\Phi = I.A\cos\theta/4\pi d^2$.

From NLTE flare model calculations (models F1, F2, F3 from Machado et al. 1980; Avrett et al. 1986; and models H1 and H4 from Houdebine 1992), we derive a simple relation between the Hα surface intensity $I\alpha$ and the column mass M for the line formation corresponding to the base of the transition region temperature rise $M = 2.3\,10^{-10} I\alpha$. This relation holds well between values from model F1 ($M = 4\,10^{-4}$ g cm^{-2} and $I\alpha = 2\,10^6$ erg cm^{-2} s^{-1} sr^{-1}) to model H1 ($M = 0.6$ g cm^{-2} and $I\alpha = 2\,10^9$ erg cm^{-2} s^{-1} sr^{-1}).

Then the hydrostatic pressure P and typical mass density ρ for the Hα formation region can be estimated for both flares using the relation $P = \mathrm{Mg} = \rho(kT/\mu\mathrm{m} + v^2/2)$ with $g = 2.5\,10^3$ cm s^{-2} on the subgiant primary surface, $T = 8000$ K, k and m being the Boltzmann and proton mass constants and the mean molecular mass $\mu = 1.2$ assumed at chromospheric temperatures. Here $\rho v^2/2$ is the dynamic pressure in the Bernouilli equation. The turbulent velocity v is estimated to be 50 km s^{-1} from the minimum Hα broadening after deconvolution from the opacity broadening. We find $v^2/2 = 4\,10^{13}$ cm^2 s^{-2}, some 30 times larger than the thermal term kT/μm, indicating that the pressure is dominated by the dynamic term during the flare. From this we can derive the mass density. These parameters are given in Table 7.

We thus find that the Hα formation occurs at large column mass, representative of photospheric conditions, which is consistent with the observation of a white-light flare. We can also derive densities up to 2–3 10^{13} cm^{-3} and H column densities of 3–5 10^{23} cm^{-2} for the flare Hα emitting component. We checked that for those densities, the Hα Stark broadening is small compared to the observed broadenings, and does not affect the previous analysis.

Table 7. Hα fluxes, column mass and density for MUSICOS white-light flares

	Xinglong	ESO
Hα equivalent width excess (Å)	0.95	2.7
Hα peak flare flux (erg cm^{-2} s^{-1})	$55\,10^{-12}$	$150\,10^{-12}$
Hα surface intensity Iα (erg cm^{-2} s^{-1} sr^{-1})	$2.3\,10^9$	$3.9\,10^9$
Derived column mass M (g cm^{-2})	0.53	0.9
Hydrostatic pressure $P = \mathrm{Mg}$ (dyn cm^{-2})	1325	2250
Massic density ρ (g cm^{-3})	$3.1\,10^{-11}$	$5.6\,10^{-11}$

10.3. Kinetic energy budget for the flare

From the observed velocity flows derived in the Hα profile, we can estimate a kinetic energy flux as $P_{kin} = \rho.v.A(v^2 + \xi^2)/2$, where ρ is the mass density, v is the mean velocity, ξ is the rms turbulent velocity, and A is the physical flare area. One can estimate the velocity from the observed average profile Doppler shifts $v_{obs} = v\cos\theta$, assuming that the motion is normal to the stellar surface at the flare loop footpoint and the turbulent velocity $\xi^2 = 3\sigma_v^2$ from the observed velocity full width half maximum ($\sigma_v = \mathrm{FWHM}/2.35$) broadening assuming isotropic turbulence. For the different phases of the flares spectroscopically observed at Xinglong and ESO in Hα, we derive the kinetic energy flux and budget in Table 8.

We assume that $\cos\theta = 0.18$ and 0.3 for the Xinglong and ESO flares, respectively, consistent with the previous discussion. We do not have a direct measurement of the density of the Hα emitting material for all components. We scale it to the total density from the ratio between the flare component flux to the peak Hα flux. We then derive the kinetic energy input by multiplying by the observed time duration of these flare component phases.

For the Xinglong flare we find the same order of magnitude ($-2\,10^{37}$ erg) for the kinetic energy budget during the impulsive phase and the radiative losses, but the comparison cannot be made as quantitative as for the ESO flare, due to the occultation during the gradual phase. For the ESO flare, we find a typical kinetic energy input of $+2\,10^{38}$ erg, which is approximately equal to the derived radiative loss budget. The kinetic energy output during the impulsive phase may be considered a lower limit as hotter material from chromospheric evaporation would not give a significant signature in Hα. This comparison indicates an equipartition between kinetic and radiative energy, as suggested in previous studies (see Linsky et al. 1988).

We give in Table 9, a summary of physical parameters derived for the two white-light flares, based on the previous analysis of the MUSICOS campaign observations.

10.4. Magnetic loops and energy in RS CVn stars

We present our interpretation for the observed energy budget in a flaring magnetic arcade geometry, and discuss possible implications for flare energy transport mechanisms. The detailed time behaviour of the line and continuum fluxes, and of the line profiles during these two flares provide constraints on flare models

© European Southern Observatory • Provided by the NASA Astrophysics Data System

1994A&A...292..543F

Table 8. Kinetic flux and budget for components of MUSICOS flares

	Time	v_{obs} (km s^{-1})	σ_v (km s^{-1})	EW(Hα) (Å)	$P_{kinetic}$ (10^{33} erg s^{-1})	E_{kin} (10^{36} erg)
Xinglong flare, 14 Dec.						
blue wing	15:26–15:56	−55	70	0.5	−5.1	−9.2
	15:57–16:27	−65	105	0.4	−7.3	− 13.8
ESO flare, 15 Dec.						
Excess blue wing	2:04–2:45	−230	150	0.17	−17	−40
Flash broadening	2:50–3:10	20	100	0.4	0.2	0.3
Core excess	3:15–3:50	20	55	1.4	0.25	0.5
Red excess	3:00–3:30	150	100	0.15	4.1	7.5
	3:30–4:00	250	140	0.35	43	78
(extrapolated)	4:00–4:30					(50)
Gradual phase	4:30–24:30	25	100	1.5	0.63	60

Table 9. Summary of physical parameters for the HR 1099 MUSICOS flares

Date of the flare	1989 December 14	1989 December 15
Start time of the flare	14:00 UT	01:00 UT
Time of the flare peak	17:00 UT	03:20 UT
Phase of the flare peak	0.45	0.56
Peak $(V, B-V, U-B)_F$	7.56, 0.43, −0.61 mag	6.19, 0.16, −0.65 mag
Peak luminosity (3100–5900 Å)	1.65 10^{33} erg s^{-1}	14 10^{33} erg s^{-1}
Projected equivalent area	8.5 10^{21} cm^2	14 10^{21} cm^2
Foreshortening cos θ	0.18	0.3
Flare physical area	1.8 10^{22} cm^2	1.9 10^{22} cm^2
Integrated losses (3100–5900 Å)		
(observed)	8 10^{36} erg	1.2 10^{38} erg
(limb corrected)	28 10^{36} erg	2.85 10^{38} erg
Balmer line losses	25 10^{34} erg	130 10^{34} erg
Hβ	4 10^{34} erg	20 10^{34} erg
Hα	6.5 10^{34} erg	35 10^{34} erg
Flare occultation	Phase 0.46, decay time 50 mn	
Hα rise timescale	2 hours	1.9 hours
Hα decay timescale	3.6 hours partial occultation	1/e decay time 21.5 hours
Kinetic energy flux	−2 10^{37} erg (flare rise)	2 10^{38} erg (total)

of mass motions, ejections and coronal condensations. The behaviour of the post-flare phase in the far-ultraviolet emissions, and in the mid-UV resonance lines of atomic and singly-ionised magnesium, must be discussed in the context of the optical tracers of the pre- and post-flare phases.

Solar flare loops are typically smaller than a few 10^9 cm in size. For RS CVn stars, previous analysis led to loop lengths of the order of 6–9 10^{10} cm for an ultraviolet flare observed on HR 1099 by Linsky et al. (1988). This is consistent with the variation of the pressure and density scale height as inverse of the gravity. Thus loops of size comparable with the stellar radius can be expected, as also shown by spectral imaging in the Hα line (Foing et al. 1990) based on profiles showing Hα emission at velocity position indicating circumstellar rather than surface features, and a preferential distribution near the Lagrange points between and outside the stars. We estimate the available magnetic energy available in a magnetised corona of extension $H = \alpha R$ around the primary, where R is the radius and α a constant to be determined, assuming a typical value for the magnetic field given at the surface by equipartition ($B^2/8\pi = P_{gas}$): $E_{mag} = 0.5B^2R^2\alpha R$. In the case of HR 1099 primary, $R = 3.9\,R_\odot$ and equipartition field $B = 1$ kG, this leads to $E_{mag} = 10.2\alpha 10^{39}$ erg.

However, we do not expect all the corona to be magnetised at this level, as we have evidence for discrete active regions such as photospheric spots or chromospheric plages. Thus, it is more reliable to estimate the magnetic energy content due to loops connecting different polarities. For a simple loop with foot-point cross-section A (or a series of loops in an arcade with equivalent foot-point cross-section), the corresponding available magnetic energy is $E_{mag} = A\pi\alpha R.B^2/8\pi$. For a decrease of magnetic field with height, for instance a quadratic varia-

© European Southern Observatory • Provided by the NASA Astrophysics Data System

1994A&A...292..543F

tion of the field along the expanding tube from Bo at the foot-point to Bmin at height $H = \alpha R$, one finds a magnetic energy $E_{mag} = HAB_0^2/8(1/3 + 2B_{min}/3B_0)$. This gives the maximum of free energy that can be liberated during the flare. Flares are thought to be produced by the annihilation of a portion of the magnetic field of a loop, the fraction depending on the configuration. The shear of an arcade of loops tends to raise E_{mag} in the system until the occurrence of a reconnection or an interconnection with another loop system. If one assumes that the foot-point cross-section can be estimated from the physical area derived from the V and $B - V$ magnitudes for the flares, one finds that $E_{mag} = 2\alpha(B/1\,\mathrm{kG})^2(1+2B_{min}/B_0)10^{38}$ erg. We can take as an estimate of the loop height H the equivalent size of the derived flare area $\sqrt{(A/\pi)} = 750$ Mm (or $\alpha = 0.27$) and assuming a B_0 magnetic field of 1 kG. This gives $E_{mag} = 5$–$15\ 10^{37}$ erg depending on the opening of the magnetic field. By comparing to the estimated radiative losses of $2\ 10^{37}$ erg for the first flare, we see that such a system of magnetic loops would liberate enough magnetic potential energy to explain the observed radiative losses. This is marginally insufficient to explain the energetics of the second flare (ESO flare) for which radiative and kinetic energy are at least $2\ 10^{38}$ erg each. Van den Oord (1988) calculated the maximal storage of energy when the filament is located between both binary components. He calculates an available energy:

$$W = 4\ 10^{37}(L/Ro)(a/Ro)^2(B/1\mathrm{kG})^2 = 5.3\ 10^{39}(L/Ro)(B/1\mathrm{kG})^2\,,$$

where L is the length of the filament, and a is the binary separation (equal to $11.5Ro$ for HR 1099). Taking for the filament a typical size L (750 Mm) as derived from the flare area, the energy stored can be up to several 10^{39} erg, sufficient to explain the energy budget of the second flare.

10.5. Flaring magnetic arcades and double ribbon flares

For both flares, we propose a model in which an arcade of coronal loops is excited and then cools quasi-statically in the decay phase. This is based on similar rise times for the two events, even though the volumes involved seem very different. Such a situation could be explained by an instability in the active region filaments. The flare observed on HR 1099 had radiative losses that appears to be as large as 10^5–10^6 times the energy found for solar two-ribbon flares. We also find possible evidence of the destabilisation of a magnetic loop by noting possible quasi-periodic U variations between 14 and 16 UT after a precursor event on 12:30 UT during the 14 December event (see Fig. 5).

We consider now the energy of a filament or a coronal condensation forced magnetically to corotate with the binary system. Its energy can be described, in the corotating frame, as the sum of equivalent centrifugal potential, the gravitational terms associated to the two components, and the magnetic energy term. If a_1 ands a_2 are the stars distances to the centre of mass G, Ω the rotation rate, x the distance along the star centres, and the system rotation axis going through the center of mass G and perpendicular to the star centres, then the potential energy of the system is:

$$E = -0.5(x^2+y^2)\Omega^2 - GM_1/[(x-a_1)^2+y^2+z^2]^{1/2} - GM_2/[(x+a_2)^2+y^2+z^2]^{1/2} + E_{mag}\,.$$

The Lagrange points, where rotational and gravitational forces cancel, are unstable if only these forces are considered. However, the magnetic forces allow matter to stabilise above stellar surfaces. A magnetic loop exerts on the filament magnetic tension, a restoring force that can be described as deriving from an harmonic potential $E_{mag} = 0.5k(x - x_0)^2$, where the elastic parameters can vary slowly under the effect of sub-photospheric forces tending to raise the height, x_0, of the loop or to modify the rigidity, k, of the configuration.

Different formulations corresponding to different boundary conditions or loop geometries can phenomenologically describe this situation. For instance, one can consider the force exerted on the material as tension $A_0(B^2/4\pi).(D/R_c)$, for a loop constrained to a given basis separation D at photospheric level and A_0 the photospheric area at the footpoint. The height of the top of the loop can thus be described as $x_0 - R = R_c[1-(1-D^2/4R_c^2)]$, in that case one obtains a stable configuration for a given height . These forces can act to raise loops and their contents against the gravitational potential. When the magnetic field approaches the Lagrangian point, the loop can fill in with additional matter, even at enhanced densities. The loop can thus increase its size until the magnetic force cannot balance the gravito-rotational forces, or until a reconnection is possible to a lower magnetic free energy configuration. Plasmoid material is then expelled at the apex.

Much of the liberated energy can be transformed into kinetic energy causing coronal mass ejections into the corona, as indicated by the blueshifted absorption wing in Hα over a large range of velocities in the two flares. The first spectrum obtained at ESO on the 15 Dec. flare might be itself already affected by the filament absorption if one considers the exceptionally low Hα equivalent width for this preflare spectrum. Part of the material in the remnant loop, that is no longer stable, can condense and flow down almost ballistically along post-flare loops. It will appear with a low and defined velocity, as observed in the narrow post flare absorption feature in Hα. Upon hitting the surface, this material can liberate additional material, depending on the mass involved.

10.6. Flare energy transport mechanisms

Three types of theories have been proposed to explain how the flare energy, which is released in the upper corona by magnetic field reconnection, is transported down to the lower layers. These theories assume either beams of energetic particles, thermal conduction or shock waves. Magnetic reconnection generate currents that can accelerate electrons and particles. These can penetrate down into the chromosphere and photosphere, if the beam is sufficiently energetic. Brown (1971) gives the stopping length for an electron with energy E(keV) as $h = 1.5\ 10^{17}E^2/Ne$.

© European Southern Observatory • Provided by the NASA Astrophysics Data System

1994A&A...292..543F

For the typical densities (10^{11} cm^{-3}) and lengths (10^5 km) inferred for the RS CVn flaring loops, one would expect that only the electrons with energy above 260 keV could penetrate down to the photosphere. Here we derive densities up to 10^{13} cm^{-3} and column densities of 10^{23} cm^{-2}, thus it seems difficult to achieve a sufficient penetration, this way. Previously, it was believed that large optical flares could not be observed in RS CVn stars if electron beams contain the dominant part of the energy, because the extended structures in these stars would stop the electrons before they could reach the photosphere. Thus flares could be observable only in transition region and coronal diagnostics. The observations of optical flares obtained with the MUSICOS campaign pose a fundamental puzzle about the role of electron beams in violent flares. Our observations may support the view that in these large stellar flares, thermal conduction is the primary physical agent that couples the coronal plasma to the lower emitting layers down to the photosphere (Mullan 1976). Alternatively, one may be forced to consider the role of particle beams such as protons (Heritschi; 1986). Such beams could create hard X ray photons that can penetrate considerably deeper into the atmosphere. This mechanism was considered by Grinin & Sobolev (1990), who showed that a beam of 10 MeV protons produces a maximum heating rate at a column density 10^{22} cm^{-2}, and the produced photons can reach 10^{24} cm^{-2}, depositing an energy about 10 times larger. The spectral signatures of electron beams as compared to proton beams have been investigated (e.g. on Hα wings, Canfield & Gunkler; 1985). These models require observational checks, using high time resolution spectra obtained during the impulsive phase of flares, for different classes of stars.

11. Perspectives after the HR 1099 MUSICOS 89 campaign

The HR 1099 MUSICOS 89 campaign was successful, thanks to the good phase coverage and continuous monitoring allowed from the different sites. From two optical flares observed photometrically and spectroscopically, we could measure radiative losses, as well as flare dynamic signatures. We discussed the energy budget and transport mechanisms during these flares in the context of destabilised flaring loops. The Doppler imaging programme was made difficult by the moderate resolution and limited S/N of the instruments available for this campaign, and by the contamination effects due to a strong chromospheric and flaring activity during the campaign. The overall data sets analysed by different MUSICOS collaborators for the reconstruction of active surface structures or the physical modelling of the observed flares, are being used for subsequent semi-empirical modelling and theoretical interpretation in order to:

(a) obtain an image reconstruction of the photospheric and chromospheric structures using Doppler or spectral imaging techniques,

(b) correlate location and extent of active structures at different heights and temperature regimes

(c) study the vertical temperature and density structure in active regions and derive information on their energy balance, and

(d) study the energy budget, time evolution and dynamics of flares.

The scientific challenge of interleaving the *Surface structures* and the *Flare monitoring* programmes has paid off, though it involved a more difficult and careful planning. It was a complex inaugural programme, but the results have justified the overall effort of the instrumental groups and of the observers, combined with the luck of detecting two exceptional flare events on the HR 1099 system. The wide range of instrumentation used has allowed important questions to be uniquely addressed. The use of echelle spectrographs for next multi-site campaigns will be a formidable gain. The homogeneity of the data will be as crucial as the continuity of the multi-site observations, which requires in the long term a set of identical instruments and rigorous methods for data merging. Simultaneous and continuous photometric coverage appears clearly valuable, especially for the flare programme for which the information brought by a better time resolution is crucial for understanding some flare processes. Other wavelength regimes (in the radio or X-ray) should be further exploited in the next campaigns of this type, making coordinated use of facilities such as the VLA, IUE, ROSAT, EUVE, ASCA and the Hubble Space telescope.

Acknowledgements. We wish to thank those that have contributed to the MUSICOS 89 campaign, and the allocation committees of the telescopes used for this programme. We acknowledge in particular M. Alvarez, J.P. Sareyan, J. Chauville, C. Brown, P. Lemaire, H. Maitzen, A. Page, R. Vitry, S. Vogt, J.P. Zimmermann. We thank the technical and scientific staffs of the different observatories at ESO, Mac Math NSO, CFH, UH, BAO Xinglong, Crimea, Catania, OHP and IUE for their participation in the MUSICOS campaign. We thank the referee J.L. Linsky for his constructive comments and improvements in the science and the style of this paper. We acknowledge the financial support of INSU/CNRS, the Paris observatory, ESA for the MUSICOS operation and analysis, and acknowledge a CNRS/EEC grant to BHF and collaborators for an European research network (ICARUS) for programmes on "Stellar activity".

References

Allen C.W., 1973, Astrophysical quantities
Avrett E.H., Machado M.E., Kurucz R.L., 1984, in: Neidig D.F. (ed.) The Lower Atmosphere in Solar Flares
Ayres T.R., Linsky J.L., 1982, ApJ 254, 162
Ayres T.R., Judge P., Jordan C., Brown A., Linsky J.L., 1986, ApJ 311, 947
Bartolini C. et al., 1983, A&A 117, 149
Baudrand J., Böhm T., 1992, A&A 259, 711
Bopp B.W., Fekel F. Jr., 1976, AJ 81, 771
Bopp B.W. et al., 1977, A&A 82, 47
Brown J.C., 1971, Solar Phys 18, 489
Butler C.J., Rodonò M., Foing B.H., 1988, A&A 206, L1
Byrne B. et al., 1987, A&A 180, 172
Canfield R.D., Gunkler T.A., 1985, ApJ 288, 353
Catala C., Foing B.H., 1990, in: Catala C., Foing B.H. (eds.) Proceedings of the 2nd Workshop on MUlti SIte COntinuous Spectroscopy, Publications of Meudon Observatory, (Proc. MUSICOS II), p. 49

© European Southern Observatory • Provided by the NASA Astrophysics Data System

1994A&A...292..543F

Catala C., Foing B.H., Baudrand J., and 23 co-authors, 1993, A&A 275, 245 (paper I)
Char S., Foing B.H., 1989, in: Proc. Modelling the Stellar Environmentent, how and why?, p. 211
Char S., Foing B.H., Lemaire P., et al., 1990, in: Catala C, Foing B.H. (eds.) Proceedings of the 2nd Workshop on MUlti SIte COntinuous Spectroscopy, Pub. of Meudon Observatory, p. 169
Char S., May 1992, PhD, University Paris VII, Activité de Type solaire dans les étoiles froides: Diagnostics spectroscopiques Ca II de structures chromosphériques
Char S., Foing B.H., 1993, A&A 276, 69
Char S., Foing B.H., Jankov S., 1993, A&A, (submitted)
Cutispoto G., 1990, A&AS 84, 397
Cutispoto G., Rodonò M., 1992, in: Byrne P.B., Mullan D.J. (eds.) Surface Inhomogeneities on Late-type Stars, Lecture Notes in Physics, Springer-Verlag, p. 265
Fekel F.C., 1983, ApJ 268, 274
Felenbok P., Guérin J., 1987, in: Cayrel de Strobel G., Spite M. (eds.) Proceedings of the 132nd IAU symposium, Paris, p. 31
Foing B.H., 1989, Solar Phys. 121, 117
Foing B.H., Char S., Jankov S., Houdebine E.R., 1990, in: Proceedings ERAM, New Windows to the Universe, Cambridge University Press
Foing B.H., Char S., Jankov S., 1990, in: Catala C. Foing B.H. (eds.) Proceedings of the 2nd Workshop on MUlti SIte COntinuous Spectroscopy, Publications of Meudon Observatory, (Proc. MUSICOS II), p. 49
Foing B.H., Houdebine E.R., Char, S., et al., 1994, (in preparation)
Grinin V.P., Sobolev V., 1989, in IAU Colloq. 104, Poster papers, Catania Special Volume, p. 297
Hall D.S., 1981, in: Bonnet R.M., Dupree A.K. (eds.) Solar Phenomena in Stars and Stellar Systems, p. 431
Heritschi D., 1986, ApJ 311, 474
Houdebine E.R., 1992, Irish Astronomical Journal 20, 213
Jankov S., Foing B.H., 1990, in: Catala C., Foing B.H. (eds.) Proceedings of the 2nd Workshop on MUlti SIte COntinuous Spectroscopy, Publ. of Meudon Observatory, p. 65
Jankov S., Foing B.H., 1992a, A&A 256, 533
Jankov S., Foing B.H., 1994, A&A, (in press)
Kinney A.L., Bohlin R.C., Neill J.D., 1991, PASP 103, 694
Landini M., Monsignori Fossi B.C., 1990, A&AS 82, 229
Linsky J.L., Ayres T.R., 1978, ApJ 220, 619
Linsky J.L., Neff J.E., Brown A., et al., 1989, A&A 211, 173
Machado M.E., Avrett E.H., Vernazza J.E., Noyes R.W., 1980, ApJ 242, 336
Mullan D.J., 1976, ApJ 207, 289
Mullan D.J., 1985, in: Hjellming H., Gibson D. (eds.) Radio stars, Reidel Publ., p. 185
Neff J.E., Walter F.M., Rodonò M., Linsky J.L., 1989, A&A 215, 79
Neff J.E., 1990, in: Catala C., Foing B.H. (eds.) Proceedings of the 2nd Workshop on MUlti SIte COntinuous Spectroscopy, Publ. of Meudon Observatory, p. 35
Owen F.N., Jones T.W., Gibson D.M. (1976), ApJ Let. 210, L27
Rodonò M., et al., 1986, A&A 165, 135
Rodonò M., Byrne P.B., Neff J.E., et al., 1987, A&A 176, 267
Simon T., Linsky J.L., Schiffer F.H., et al., 1980, ApJ 239, 911
van den Oord G.H.J., 1988, A&A 205, 167
Vogt S., Penrod G., 1983, PASP 95, 565
Walter F., Charles P., Bowyer S., 1978, Nat 274, 569
Zhai D.S., Zhang R.X., Zhang X.B., et al., 1990, in: Catala C., Foing B.H. (eds.) Proceedings of the 2nd Workshop on MUlti SIte COntinuous Spectroscopy, Publ. of Meudon Observatory, p. 133
Zhai D.S., Foing B.H., Cutispoto G., et al., 1994, A&A 282, 168

© European Southern Observatory • Provided by the NASA Astrophysics Data System